Instabilities, Dynamics, and Energetics accompanying Atmospheric Layering (IDEAL): High-Resolution in-situ Observations and Modeling in and above the Nocturnal Boundary Layer

Abhiram Doddi[1], Dale Lawrence[1], David Fritts[2], Ling Wang[2], Thomas Lund[2], William Brown[3], Dragan Zajic[4], and Lakshmi Kantha[1]

[1]Smead Aerospace Engineering Sciences, University of Colorado, Boulder, CO, USA
[2]GATS, Boulder, CO, USA
[3]Earth Observing Laboratory, National Center for Atmospheric Research, Boulder, CO, USA
[4]Meteorology Division, Dugway Proving Ground, Dugway, UT, USA

Correspondence: Abhiram Doddi (abhiram.doddi@colorado.edu); Dale Lawrence (dale.lawrence@colorado.edu); David Fritts (dave@gats-inc.com); Ling Wang (lwang@gats-inc.com); Thomas Lund (t.lund@gats-inc.com); William Brown (wbrown@ucar.edu); Dragan Zajic (dragan.zajic.civ@mail.mil); Lakshmi Kantha (kantha@colorado.edu)

Abstract. The Instabilities, Dynamics, and Energetics accompanying Atmospheric Layering (IDEAL) program was conceived to improve our understanding of the dynamics of sheet and layer (S&L) structures in the lower troposphere under strongly stable conditions. S&L structures comprise thin strongly stratified "sheets" and deeper, weakly stratified "layers" that arise due to superposed larger-scale mean and gravity wave motions (Fritts and Wang, 2013), the dynamics of which previous small unmanned aircraft system (sUAS) flights were found to provide valuable insights (Balsley et al., 2018). The IDEAL field program was conducted from 24 October to 15 November 2017 at Dugway Proving Ground (DPG) Utah to target the lower troposphere S&L conditions. It employed a synergistic combination of observations by multiple, simultaneous DataHawk-2 (DH2) sUAS and concurrent ground-based profiling by an NCAR Earth Observing Laboratory Integrated Sounding System (ISS) comprising a wind profiler radar and hourly, high-resolution radiosonde soundings. Measurement intervals, vertical and horizontal extents (typically ∼5-10 km horizontally, ∼2-4 km vertically), and DH2 flight orientations were chosen based on local high-resolution forecasting, and guided by near-real-time ISS measurements once DH2 flights commenced. The UAS flights combined simultaneous vertical and slant-path profiling, and/or horizontal racetrack sampling, spanning several hours predominantly before sunrise. The UAS measured in situ winds, temperatures at high spatial and temporal resolution, and down-linked data in real time to enable near-real-time changes in DH2 flight paths based on observed flow features. The IDEAL field program performed 70 DH2 flights on 16 days coordinated with 93 high-resolution radiosonde soundings. Atmospheric modeling motivated by IDEAL observations is reported elsewhere.

Copyright statement. TEXT

1   Introduction

Under stable conditions, the vertical structure of the atmosphere is characterized by thin, strongly stable non-turbulent "sheets"
separated by thicker, less stable and often weakly turbulent "layers" (Woods, 1969, 1968; Gage and Green, 1978; Röttger and
Liu, 1978). These sheet and layer (S&L hereafter) structures are often observed in temperature, humidity, and horizontal winds
within the lower troposphere (Balsley et al., 2006, 2003; Chimonas, 1999; Mahrt, 1999; Xing-Sheng et al., 1983; Kantha et al.,
2019) and into the edge of the Stratosphere (Barat, 1982; Fairall et al., 1991; Gage and Balsley, 1980; Röttger, 1980; Woodman
and Guillen, 1974). The S&L structures are known to play an important role in the transport and mixing of heat, momentum,
and constituents (Barat, 1982; Chimonas, 1999; Dalaudier et al., 1994; Hunt et al., 1985), as well as important roles in optical
(Coulman et al., 1995) and radio wave propagation (Gossard et al., 1984; Luce et al., 2001; Röttger, 1980; Xing-Sheng et al.,
1983).

The large-scale vertical features of the layering structures have been qualitatively analyzed using monostatic and bistatic
VHF radar observations (Balsley et al., 2006, 2003; Dalaudier et al., 1994; Luce et al., 2001, 1995; Woodman and Chu, 1989).
Details have been characterized in terms of typical sheet thickness and stability, thickness of turbulent layers, Richardson
Number, and turbulence Reynolds number through in situ measurements from soundings, stationary observation towers and
tethered lifting systems (TLS) (Balsley et al., 2003, 2006; Muschinski et al., 2001a), and more recently, using aircraft (Lawrence
and Balsley, 2013; Muschinski and Wode, 1998; Scipión et al., 2016). High-resolution multipoint measurements of temperature
(Barat, 1982; Coulman, 1973; Frehlich et al., 2003; Hunt et al., 1985; Xing-Sheng et al., 1983) and VHF radar estimates
(and comparison with theoretical models) of refractive index structure function (C_n^2) (VanZandt et al., 1978; Woodman and
Guillen, 1974) have established the intermittent nature of turbulence within deep layers. More recently, quantitative aircraft
measurements of turbulence kinetic energy dissipation rate (ϵ) and the temperature structure function (C_T^2) have characterized
the small-scale turbulence features within shallow turbulent layers in the troposphere (Balsley et al., 2018; Eaton et al., 1998;
Fernando et al., 2015; Muschinski et al., 2001b; Scipión et al., 2016).

Various explanations for the prevalence of S&L structures have been proposed. Concurrent observations using VHF radars
and in situ measurements suggest that S&L are the result of multiscale gravity waves (GWs) interacting with the fine structure
(FS) of the background atmosphere (Barat, 1982; Coulman et al., 1995; Luce et al., 1995; Röttger, 1980). Some analytical
studies and numerical modeling results support this conjecture (Fairall et al., 1991; Fritts and Rastogi, 1985; Fritts et al.,
2009a; Fua et al., 1982; Sidi et al., 1988; Smith et al., 1987; VanZandt et al., 1978). More recent Direct Numerical Simulations
(DNS) achieving very high spatial and temporal resolution, primarily addressing multiscale GW and fine structure (GW-FS)
interactions in "stable" environments (Fritts and Wang, 2013; Fritts et al., 2009b, 2013), suggest that Kelvin-Helmholtz insta-
bilities (KHI), GW breaking and intrusions lead to the formation of S&L. Tjernström et al. (2009) suggested that airflow over
low-relief terrain (i.e., small-scale mountain waves) are a plausible formation mechanism for S&L in the lower troposphere.

Initial modeling exploration of formation mechanisms of S&L structures arising from superposition of convectively stable
GWs and dynamically stable mean shears, referred to as multiscale dynamics (MSD), employed an idealized high resolution
DNS (Balsley et al., 2018; Fritts et al., 2013; Fritts and Wang, 2013). The initial DNS of MSD by Fritts et al. (2013) featured

a dynamically stable monochromatic GW of amplitude $a = (d\theta/dz)_{min}/(d\theta/dz) = 0.5$ and an intrinsic frequency $\omega = N/10$. A constant mean stability N, and $Re = 50,000$ were assumed to enable instabilities and turbulence structures accompanying GW-FS dynamics that extend to very small-scales (Balsley et al., 2018; Fritts and Wang, 2013; Fritts et al., 2013). The DNS identified KHI evolving along the most highly stratified vortex sheet initiated by a propagating GW and intensifying the vortex sheet accompanying its upward displacement causing the local Richardson number to decrease below 0.25. Importantly, careful analysis of ϵ fields revealed that KHI MSD made significantly larger contributions to total ϵ than other secondary instabilities and induced S&L structures. These initial MSD DNS results, and the advancing UAS measurement capabilities, provided the motivations for the IDEAL observation program.

More recently, DNS designed to further explore KHI MSD enabled misaligned initial KHI along their axes for an assumed $Re = 5000$ and a minimum $Ri = 0.1$ (Fritts et al., 2021a, b) employed a horizontal domain to allow a periodic, approximate inertia-GW shear flow with a random initial noise field exciting KH billows that consequently led to numerous cases of "tubes and knots" (T&K) dynamics which were examined in detail by Fritts et al. (2021a) and Fritts et al. (2021b). These T&K dynamics exhibited significantly accelerated transitions to, and enhanced turbulence relative to, regions exhibiting turbulence transitions in the absence of T&K dynamics. The T&K dynamics evidently drove secondary instabilities and transitions to turbulence that were dramatically more aggressive and intense than in their absence. This DNS revealed a diversity of secondary instability dynamics exhibiting small-scale versions of larger-scale dynamics accompanying more idealized GW breaking and KHI events. The MSD DNS also predicted the emergence of small-scale KHI dynamics within induced S&L structures that emerged from the idealized initial conditions. The expected wide-spread presence of MSD, given the highly modulated local sheared environments in which they occur suggest that KHI T&K dynamics in the atmosphere are more the rule than the exception, and are likely major contributors to the small-scale dynamics and S&L structures. Similar environments have been observed to occur throughout the atmosphere to altitudes above 100 km, suggesting that MSD have major influences in driving KHI T&K dynamics and the associated turbulence and mixing throughout the neutral atmosphere. The high-resolution turbulence observations carried out as part of the IDEAL program are expected to expand such DNS studies in exploring the involvement of KHI MSD in forming and driving S&L structures and accompanying turbulence in the lower atmosphere.

Previously, estimation of turbulence dissipation rate was obtained from high-resolution radiosonde measurements in the troposphere and lower stratosphere environments (Clayson and Kantha, 2008; Gong and Geller, 2010; Wilson et al., 2011; Kohma et al., 2019). Recent advances in sensing abilities of UAS have enabled detailed turbulence observations in the lower troposphere. Proof of concept for turbulence measurements using high-cadence fine-wire and multi-hole pressure probe sensors for UAVs such as the MMAV (van den Kroonenberg et al., 2008), MASC (Wildmann et al., 2014), BLUECAT (Witte et al., 2016), SUMO (Bäserud et al., 2016), Skywalker X6 (Calmer et al., 2018), ALADINA (Altstädter et al., 2015), and OVLI-TA Alaoui-Sosse et al. (2019) have been provided through extensive testing of the measurement instruments in wind tunnels and various field campaigns limited to characterize turbulence in the boundary layer. A few examples include the CASES-99 (Balsley et al., 2003), MATERHORN (Fernando et al., 2015), and BALLAST (Bäserud et al., 2016; Båserud et al., 2014). A deeper understanding of the formation, morphology, and evolution of S&L and associated small-scale, weak, intermittent turbulence structures is hampered by current turbulence observational methods that are limited by spatial and temporal resolution, and

inadequate range and dexterity of measurement platforms (Chimonas, 1999; Muschinski et al., 2001a; Muschinski and Wode, 1998; Tjernström et al., 2009). Additionally, the single-point vertical profiles (instrumented towers, balloon borne soundings, and TLS) provide little information about the lateral scales of S&L structures (Muschinski and Wode, 1998). The limited lateral-scale characterization and the dearth of high-resolution, quantitative measures of turbulence parameters provide poor guidance for modeling studies employing high-resolution DNS.

The Instabilities, Dynamics, and Energetics accompanying Atmospheric Layering (IDEAL) project was conceived to address this limitation through a synergistic combination of precisely targeted multipoint observations using small unmanned aircraft system (sUAS) guiding DNS modeling to characterize the dynamics driving S&L structures and associated flow features. The first phase of the project featured an observational field campaign to systematically probe stable lower atmosphere conditions using multiple DataHawk-2 (DH2) UAS developed at the University of Colorado, guided by NCAR Integrated Sounding System (ISS) continuous radar profiling and hourly radiosonde profiling. Measurements were conducted employing multiple DH2, most commonly in sorties of three aircraft, for in situ profiling and horizontal and/or slant path sampling. A total of 70 DH2 flights coordinated with 93 balloon-borne radiosondes were deployed supporting the IDEAL field campaign. Additionally, an array of Surface Atmospheric Measurement Systems (SAMS) collected surface winds, temperature, and relative humidity at 2 m (called mini-SAMS) and 10 m (called SAMS) to monitor surface and boundary layer activity. Observation locations of IDEAL field measurements are shown in Figure 1. Following the field campaign, the second phase focused on high-resolution DNS modeling efforts, guided by the in situ observations, to permit more quantitative exploration of S&L formation mechanisms, evolution, and morphology.

This article focuses on the details of the observational phase that took place between 24 October and 15 November 2017 at the Dugway Proving Ground (DPG), Utah. Section 2 outlines the observation platforms used and the meteorological conditions during the campaign. Section 3 describes the measurement strategy employed. Section 4 outlines the data processing, analysis techniques employed, and data availability and from the DH2 UAS measurements. Finally, section 6 provides concluding remarks and scope for future work.
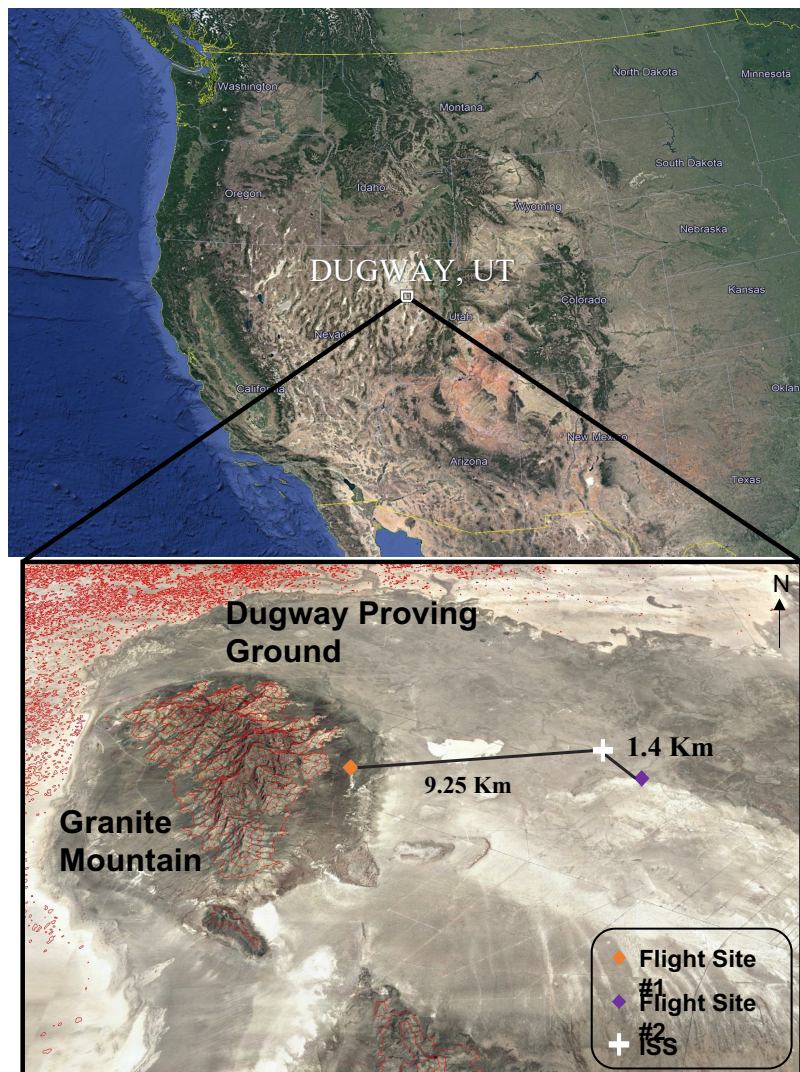
Figure 1. IDEAL field campaign location at DPG, Utah (top). The satellite image shows the DPG landscape (1320 m MSL) along with the Granite Mountain (800 m peak height) - a prominent terrain feature. The terrain map is overlaid with 50 m elevation contour lines, and locations of UAS observation sites (orange and purple diamonds) and the ISS deployment site (white cross). The satellite imagery was obtained from Google Earth 3D mapping tool.

2   Measurement Platforms and Observed Meteorological Conditions

2.1   DataHawk sUAS

The DH2 sUAS used for IDEAL measurements (see Figure 2, and Tables 1 & 2) is a product of many years of development at the University of Colorado. It is specifically designed for making high-resolution in-situ observations in the lower troposphere,

and for operations in challenging surface conditions. The precursor DH1 was used in campaigns in Peru (Balsley et al., 2013; Lawrence and Balsley, 2013; Scipión et al., 2016) and Utah (Balsley et al., 2018; Fernando et al., 2015). The DH2 was used in campaigns in Japan (Kantha et al., 2017, 2019; Luce et al., 2018a, b, 2019, 2017), Colorado (de Boer et al., 2019), and Alaska (de Boer et al., 2018). Altogether, over 650 science flights have been performed with the DH2, totaling 430 flight hours. Relevant attributes of DH2 sUAS deployed during the IDEAL field program are noted below:

– **Low cost.** At approximately \$1,000 each, many vehicles can be deployed for a campaign, enabling multiple simultaneous measurements (as employed extensively for IDEAL) or sequences of overlapping flights to provide continuous measurements over many hours. This also enables observations in marginal conditions (e.g., high winds) that would ground more expensive vehicles due to the risk of loss. Ten DH2 vehicles were brought to the 23-day IDEAL campaign.

– **Ruggedness.** The airframe is resilient foam, strengthened by a system of interior spars and flexures that absorb impacts, enabling the vehicle to "bounce" rather than break when landing on unprepared surfaces. It has a no-tail design, since these extended members are easily broken, and resilient wing trailing edges and vertical fins. It also has a rear propeller with folding blades to prevent damage to the propulsion system during landing. In the IDEAL campaign, five DH2 aircraft were used extensively, of which two were retired due to accumulated wear. No aircraft were lost.

– **Ease of operation.** A custom autopilot provides automatic launch, landing, and vector field flight control (Lawrence et al., 2008), enabling a variety of measurement strategies to be set up with ease and flown under minimal operator supervision. Flight patterns can also be changed during flight to target specific volumes of interest, e.g., based on real-time measurements—an ability that was extensively used during IDEAL to identify and more thoroughly sample turbulence fields. A bungee cord is used for launch, guided by a simple two-rail launch ramp (see Figure 2).

– **Gust-insensitive design.** The unique aerodynamic design eliminates the roll moment due to sideslip, making the vehicle point into gusts rather than roll away from it, enabling well-behaved flight in high-wind and strong turbulence conditions. Normally, flights are not performed when surface winds exceed $10\,\mathrm{ms^{-1}}$, or predicted winds aloft exceed $15\,\mathrm{ms^{-1}}$. The vector field guidance uses a wind-aware algorithm to stabilize flight even when wind speed exceeds airspeed. During IDEAL, synoptic winds above $3000\,\mathrm{m}$ typically exceeded $20\,\mathrm{ms^{-1}}$ which limited the flight ceiling to this altitude.

– **Flexible sensor interfacing.** The custom DataHawk autopilot provides multiple serial interfaces (7 UART, 3 I2C, 4 SPI), enabling a variety of sensors to be supported, and their data stored on-board (micro SD card), and telemetered to the ground station for real-time display. Tables 1 and 2 provide details of the sensors employed for IDEAL. Sensors can be installed at various locations in the body or the wings of the airframe without altering the flight dynamics.

– **Efficiency.** Flight durations exceed 80 min nominally, making altitudes of 5 km above a ground launch accessible with a typical $2\,\mathrm{ms^{-1}}$ ascent/descent rate, and a lateral range (out and back) of 30 km at a nominal airspeed of $15\,\mathrm{ms^{-1}}$.

Figure 2. DH2 sUAS ready for launch at DPG during the IDEAL campaign.

For IDEAL, the DH2 was configured to make the following in-situ observations.

145   1. **Measurement location and time.** A UBlox M8N single-frequency GPS receiver provides horizontal position data and time at 5 Hz cadence. Altitude measurement is refined in post-flight analysis, to obtain high-vertical resolution, by calibrating the higher rate of response (100 Hz) barometric pressure altitude against the low-rate (~ 5 Hz) GPS altitude. Similarly, sensor measurement times are recorded at high-resolution by calibrating 10 microsecond microprocessor timer ticks to GPS time of week (TOW) data in post-flight time-alignment procedures.

150   2. **Mean atmospheric state.** Temperature and relative humidity (T/RH) are provided by a Sensirion SHT-31, located in the flow stream inside a cylindrical shroud, mounted above the vehicle as shown in Figure 2. Pressure is provided by a TE MS5611 absolute pressure sensor, located in an unsealed compartment within the foam aircraft body.

    3. **High-resolution temperature.** A custom (coldwire) thermometer uses a five micrometer diameter platinum wire to detect fine-scale temperature variations in the flow. With a time constant of 0.5 millisecond and a sampling rate of
155   800 Hz, temperature variations at wavenumbers of ~ 25 m^{-1} can be detected at the nominal 15 ms^{-1} airspeed. The high-resolution temperature measurement is calibrated against the collocated (but slow) SHT temperature (to kelvin) by employing linear least squares regression in post flight analysis and used with high-resolution altitude to obtain high-vertical resolution potential temperature θ. Spectral analysis is also used to fit inertial sub-range power spectral density models to provide estimates of the turbulent temperature structure parameter C_T^2 (Luce et al., 2019).

4. **High-resolution airspeed.** A custom pitot-static tube and a TE MS4515 differential pressure sensor provide 800 Hz airspeed data that is calibrated to ms^{-1}. Wavenumber resolutions similar to temperature fluctuations are obtained in velocity variations also, and spectral estimation methods are used to derive turbulent kinetic energy dissipation rate ϵ. Filtered airspeed data are also used to estimate winds (described below). In addition, a custom (hotwire) anemometer uses a second 5 micrometer diameter platinum wire to detect fine-scale velocity variations, and these are also used to estimate ϵ, but at a higher confidence level due to the absence of motor vibration artifacts that typically appear in the pitot velocity spectra at high frequencies.

5. **Horizontal Wind.** Vehicle GPS velocity is combined with pitot airspeed and vehicle attitude to produce estimates of the horizontal wind at 1 Hz cadence in post flight analysis (Lawrence and Balsley, 2013).

6. **Atmospheric stability.** The Brunt-Vaisala (buoyancy) frequency is evaluated using vertical gradient of high-resolution potential temperature θ.

7. **Forcing conditions.** Destabilizing horizontal wind shear is assessed relative to the background layer stability via the gradient Richardson number, derived from the horizontal mean wind gradient with altitude, and the local buoyancy frequency.

DH2 Characteristics		DH2 Capabilities	
Wingspan	1.3 m	Airspeed	10-20 ms^{-1}
Mass	1.3 kg	Duration	80 minutes
Vehicle Cost	$1000	Range (one way)	60 km
Sensor Cost	$400	Altitude (balloon Drop)	6 km AGL
Design	Flying wing, rear propeller	Altitude (ground launch)	5 km AGL
Telemetry	IEEE 802.15.4, 900 MHz	Turning radius	> 50 m
Propulsion	Electric, folding propeller	Climb rate	< 3 ms^{-1}
Autopilot	Custom M4	Downlink throughput	> 1500 bytes per second
Control	Auto, operator supervised	Downlink update rate	10 Hz
Power	11 V LiPo, 7600 mAhr	Sensor sampling	up to 800 Hz
Construction	Polypropylene foam	Data storage (on board)	Micro SD card

Table 1. Characteristics of the DH2 sUAS.

Type	Resolution	Accuracy; Range	Time Constant; Cadence	Notes
Hor. Location (GPS)	10 cm	10 m; worldwide	0.2 s; 5 Hz	Real time
Altitude	10 cm	20 cm; -1 km to 20 km MSL	1 ms; 100 Hz	Post flight calibration
Time (GPS)	1 ms	0.2 s; 1 week	0.2 s; 5 Hz	Real time
In-situ temperature	0.1 °C	2 °C; -60 °C to +40 °C	5 s; 10 Hz	Real time
Rel. humidity	0.01 %	4 %; 0 % to 100 %	8 s; 10 Hz	Real time
Airspeed	0.05 ms^{-1}	0.2 ms^{-1}; 10 ms^{-1} to 20 ms^{-1}	5 ms; 800 Hz	Post flight calibration
Coldwire temperature	0.003 °C	2 °C; -60 °C to +40 °C	0.5 ms; 800 Hz	Post flight calibration
Hotwire velocity	0.01 ms^{-1}	0.2 ms^{-1}, 10 ms^{-1} to 20 ms^{-1}	0.5 ms; 800 Hz	Post flight calibration
C_T^2	10^{-6} m$^{-2/3}$K^2	10^{-5} m$^{-2/3}$K^2; 1.0 m$^{-2/3}$K^2	1 s; 1 Hz	Post flight calibration
ϵ	10^{-7} m^{2}s^{-3}	10^{-6} m^{2}s^{-3}; 0.1 m^{2}s^{-3}	1 s; 1 Hz	Post flight calibration
2D vector wind	0.05 ms^{-1}	0.5 ms^{-1}; 0 ms^{-1} to 30 ms^{-1}	0.1 s; 1 Hz	Post flight calibration
IR temperature	0.1 °C	5 °C; -40 °C to +40 °C	0.1 s; 10 Hz	Real time

Table 2. Sensing Capabilities of the DH2 sUAS used for IDEAL program.

2.2 Integrated Sounding System (ISS)

An Integrated Sounding System (Parsons et al., 1994) was deployed to monitor the large-scale wind and thermodynamic environment, in proximity to the UAV measurements. The ISS consisted of a Vaisala MW41 radiosonde sounding system, a LAP3000 915 MHz radar wind profiler, and Lufft WS700/WS800 surface meteorological sensors on a mast at 2 and 10 m. Ninety-three balloon-borne RS41-SGP radiosondes were launched between 3:00 AM and 7:00 AM LT at 30 to 60 min intervals every night, providing five to nine soundings each measurement day.

The ISS automatically ingests surface observations from a set of reference sensors (T/RH, and wind using Lufft WS700 and pressure using Vaisala PTB210) at 1.8 and 3 m. To achieve frequent soundings (< 60 min apart), communications were terminated well before balloon burst (at 12 km) to enable launch preparations for subsequent soundings. The balloon Helium volume was adjusted to achieve a median ascent rate of ~ 3.5 ms^{-1}.

The LAP3000 915 MHz radar wind profiler was operated in a low-height range mode to provide data at 60 m intervals between 200 m to 4.5 km AGL. Due to the dry conditions, winds were measured only up to 2 km on most days. The radar employed five beam directions and raw Doppler spectra were recorded every 30 s. Eastward and northward wind components were calculated from spectral moments averaged over 30 min.

Time-altitude data from radiosondes and the wind profiler were relayed hourly to the UAS flight deployment team to aid in-flight planning. Examples of ISS observations on 6th November 2017 are shown in Figure 3. Wind profiler data were used to monitor relevant events like precipitation (descending features in signal-to-noise ratio (SNR)), low-level jets (midnight at $\sim$2 km), convective instabilities, and KHI.
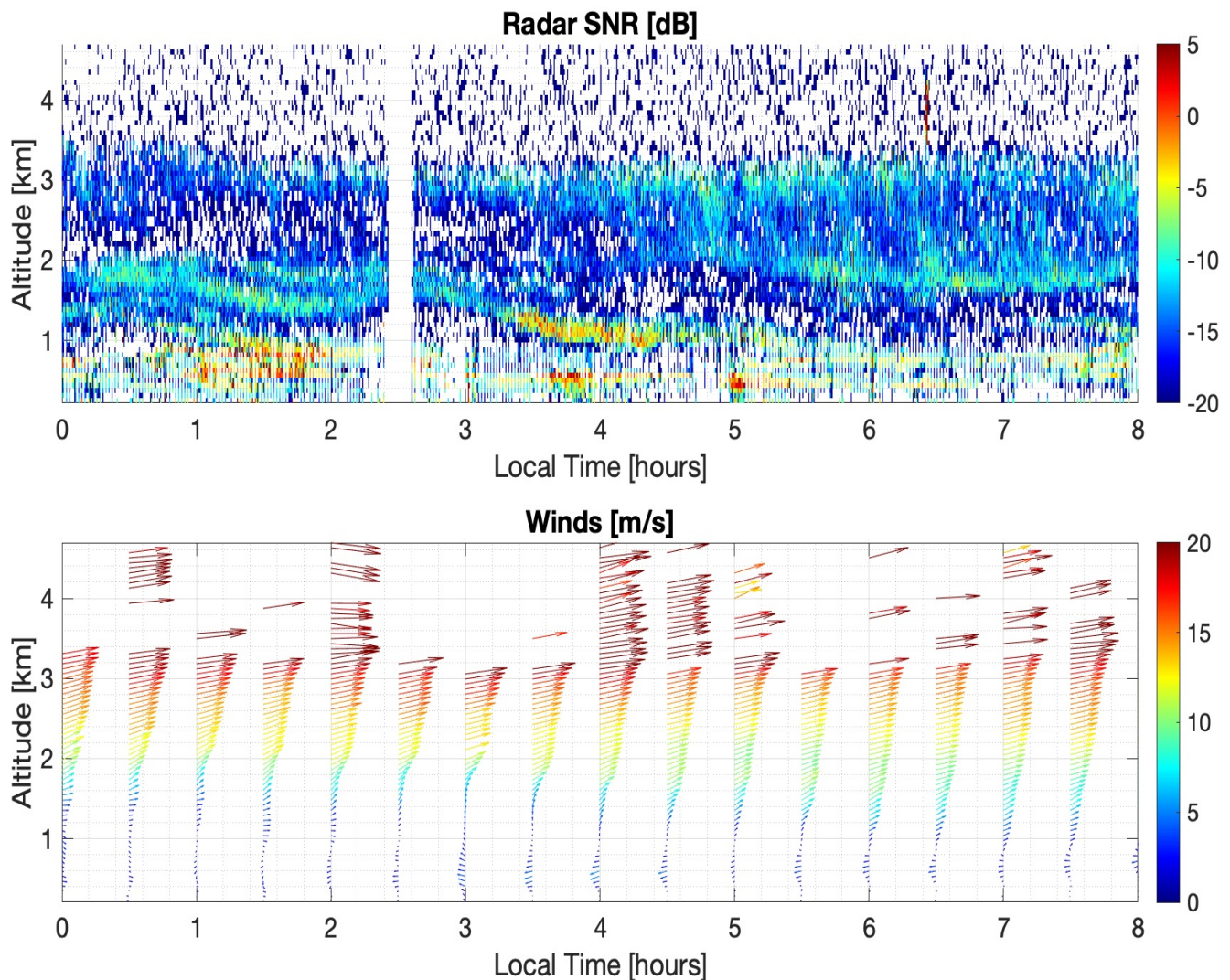
Figure 3. Example measurements by the radar wind profiler showing SNR (top) and wind barbs (bottom) for the 6th of November from 0000-0800 LT. The radar is briefly turned-off periodically for maintenance - seen as a pause between 0200-0300 LT.

2.3 Campaign Meteorological Conditions

Weather forecasts for sUAS flight planning were provided by the DPG Meteorology Division. Weather briefings consisted of 2-day forecasts from the Four-Dimensional Weather System (4DWX), and the most recent observations of surface and upper-level conditions obtained from the DPG MET instrumentation. 4DWX uses the advanced research version of the Weather Research and Forecasting (WRF) model to predict the weather conditions at the US Army Test and Evaluation Command (ATEC) ranges (Knievel et al., 2017; Liu et al., 2008). The system is a product of collaboration between ATEC and NCAR. The local surface conditions were obtained using a network of towers that includes 31 SAMS and 50 mini-SAMS. Each SAMS reports 5 min

averaged wind speed and direction at 2 m and 10 m, temperature, and relative humidity (T/RH) at 2 m, and precipitation. The mini-SAMS towers provide additional 10 m T/RH measurements with average values reported every minute. Doppler radar wind profilers provided real-time wind profiles from 120 m up to 5 km. The forecasts included expected synoptic-scale patterns, for example, expected times of frontal passage, development of surface inversions, and cloud cover.

During the campaign, DH2s were flown between 2 and 8 AM LT to sample the evolution of nocturnal atmospheric conditions. Weather briefings were provided to the team each day at 0:30 AM, so that launch sites and deployment strategies could be specified based on the most recent information. Observed T/RH, and winds from all the soundings throughout the campaign are shown in Figure 4. Conditions were mostly dry with occasional evening precipitation. Surface winds during the first week of the campaign (24 October to 1 November 2017) were consistently strong from the South (see bottom right panel in Figure 4). Thereafter, surface winds were consistently from the North. The 4DWX model predicted Northerly surface winds in the valley for the last two weeks of the campaign, and the wind forecasts agreed closely with the DPG MET 449 MHz wind profiler measurements. Predicted surface temperatures were between 0 and -5 °C for most nights.
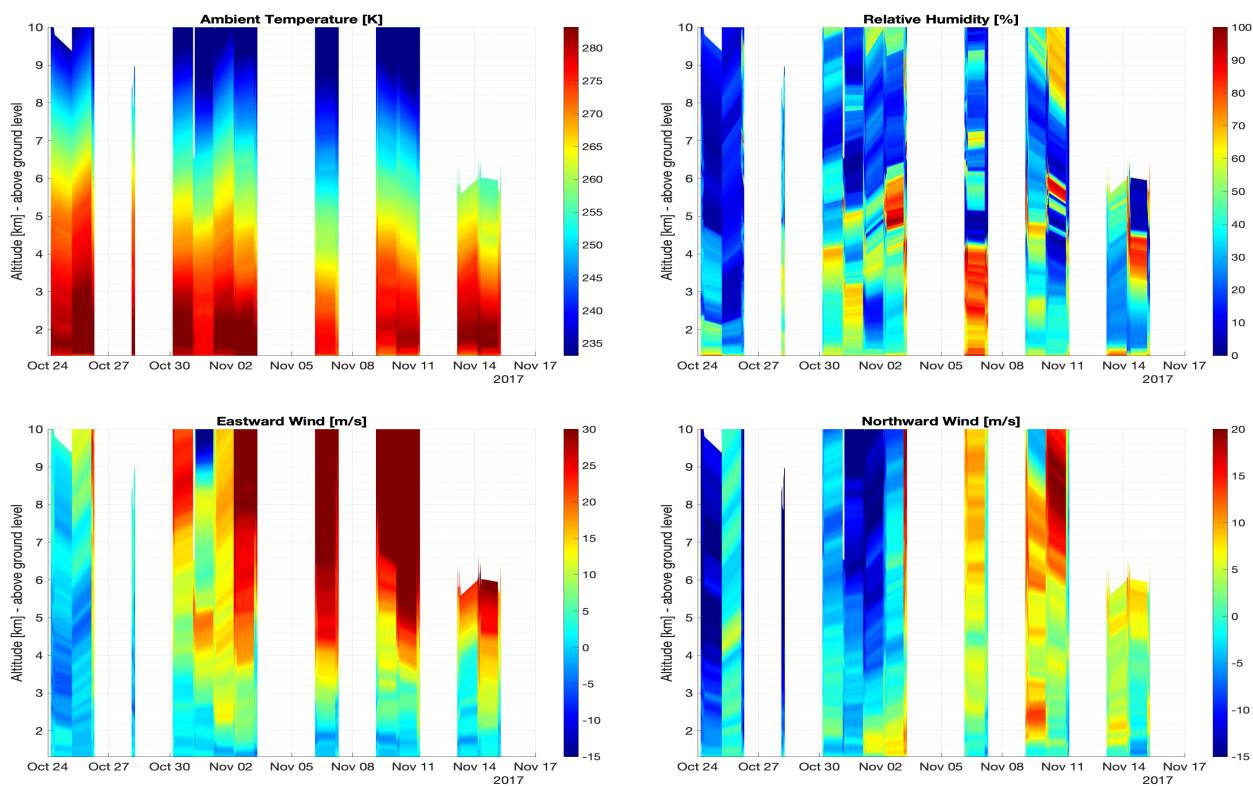
Figure 4. Vertical profiles of temperature (top left), humidity (top right), Eastward and northward winds (bottom: left and right) measured by 93 radiosondes deployed during IDEAL. Note: communications with some radiosondes were terminated early (e.g. 14th November) to facilitate a faster launch cadence.

The stable nocturnal boundary layer was shallow on most nights (~ 75 m), but occasionally increased to 200 m. Directional shear was frequently observed between the surface and altitude of 2 km. A weak westerly nocturnal jet was often observed at 2 km. Strong speed shears observed above 2 km resulted in infrequent KHI. The background atmosphere was statically stable ($N^2 > 0$) on most nights, with occurrences of stability and humidity sheets at various altitudes separated by weak, intermittent, and sporadic turbulence events.

3   Observational Strategy

The IDEAL measurement program was designed to take advantage of the high-spatial resolution, range, and dexterity of DH2 aircraft to provide high-resolution in-situ observations of S&L structures and their evolution under stable boundary layer and lower troposphere conditions. The low cost and ease of operation of DH2 sUAS discussed in Section 2.1 enabled simultaneous multi-path measurements intended to quantify local S&L flow evolution, scales, and the dynamics underlying their small-scale structures. Because in-situ measurements are necessarily sparse, DH2 trajectories were designed to provide successive, multiple-DH2 sampling of local flows along horizontal, inclined, and spiraling vertical flight paths sampling common volumes over tens of minutes.

Flight planning relied predominantly on 4DWX weather forecasts and local ISS and SAMS measurements described in Section 2.2. Evolution of predicted winds and the thermodynamic state of the synoptic-scale flow were used to identify the likely most favorable site for DH2 measurements each day. The two flight operation sites (marked 'Flight Site 1' (FS1) and 'Flight Site 2' (FS2) in Figure 1) were located on the eastern flank of Granite mountain and in the central portion of the valley, respectively. FS1 and FS2 were chosen to be upwind of the ISS deployment site for two different wind conditions. Flight operations were conducted from FS1 on days when the predicted surface winds were from the southwest-west, and the forcing was at least as strong as 8 ms^{-1} to 10 ms^{-1}. This maximized the likelihood of observing mountain wave influences on S&L structures due to Granite mountain at FS1, and accompanying fine-structure interactions leading to S&L dynamics. Flight operations were conducted from FS2 on days when the predicted winds were from the south and relatively weak.

Most recent radiosonde winds and temperatures guided the choice of measurement location and characterized the S&L structures at coarse vertical resolution. An example of the real-time radiosonde data relayed to the measurement team on 6 November 2017 is shown in Figure 5. Periodic soundings monitored the spatial variability, intermittency, and temporal evolution of the layered structures at coarse vertical resolution and contributed to go/no-go decisions for DH2 flight sorties based on the prospects for encountering interesting dynamics while avoiding high-wind conditions.
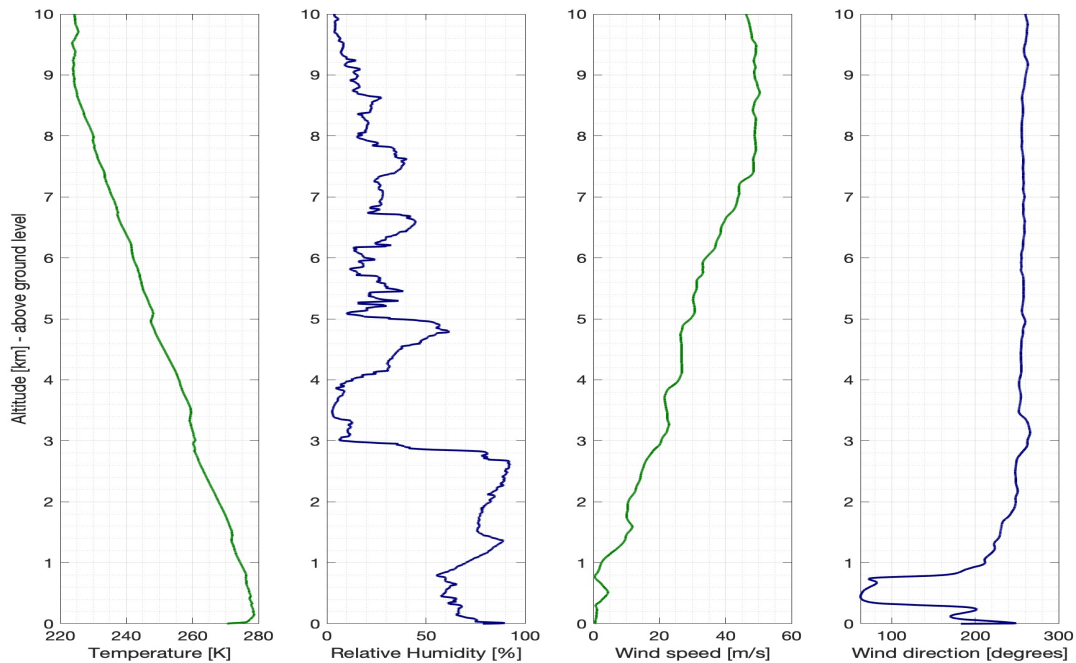
Figure 5. Altitude profiles of horizontal wind speed, direction, temperature, and relative humidity from a sample radiosonde launch at 0000 LT on 6 November 2017.

Over a span of 23 days, a total of 18 flight sorties from FS1 and 13 sorties from FS2 were performed in co-ordination with 93 periodically launched radiosondes. Rapidly changing atmospheric features around Granite Mountain often resulted in sorties containing between one and three DH2 aircraft each. Horizontal wind speeds above 3000 m frequently exceeded 15 ms^{-1} which limited the flight ceiling to this altitude. Figures 6 and 7 show the 3D contour of Granite Mountain overlaid with the DH2 flight trajectories for the two sorties carried out on 6 November 2017. The sorties shown in Figures 6, 7, and 8 sought to investigate the temporal evolution of multiple layers at different altitudes with measurements that were spaced evenly in time. A typical DH2 flight sortie during IDEAL consisted of one vertically sounding aircraft (such as A1 in figures 6, 7, and 8) flying a helical pattern of 100 m radius with nominal airspeed ranging between $14 - 18 \text{ ms}^{-1}$ and ascending/descending between $1 - 4 \text{ ms}^{-1}$. Each sortie also consisted of laterally sounding aircraft (such as A2 and A3 in figures 6, 7, and 8). The trajectories of lateral sounding aircraft in each sortie varied depending on the conditions relayed by recent radiosonde data and on the conditions observed by A1. Generally, the lateral aircraft (one or two - depending on the sortie; labelled A2 and A3 in Figures 6 and 7) were steered to concentrate on a particular turbulent layer evolution, if any such was identified in the sensor data relayed by A1. The lateral aircraft spanned 1.5 km and the racetracks oriented along the horizontal wind direction while slowly ascending and descending through a narrow altitude range to observe spatial and temporal variability in the layer. Table 3 lists the date, flight launch site, the time, the ceiling and measurement strategy for each DH2 flight for all sorties carried out during the IDEAL program. The overview plots of T/RH, static pressure, wind speed and direction, 3D GPS position, and

velocity data along with the flight notes for each sortie are available for download on the IDEAL project preliminary analysis

255 web page hosted by the University of Colorado (see Section 4).
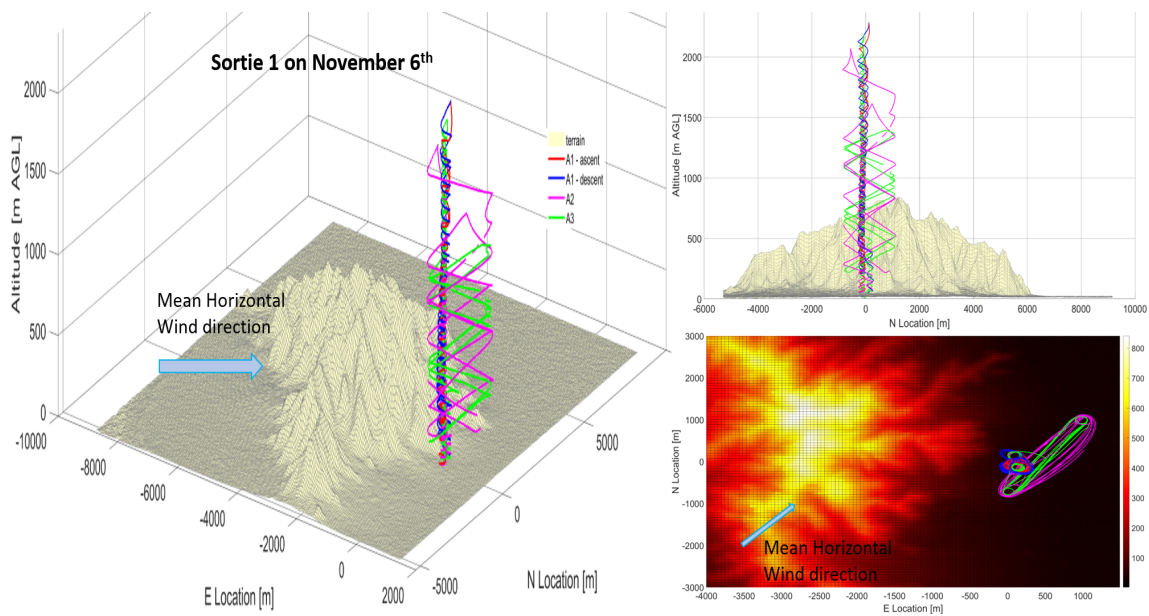
Figure 6. (Left and top right panels) Plots depicting the trajectories of the three aircraft A1, A2, and A3 deployed at FS1 for sortie 1 on 6 November 2017. The low-relief terrain feature is Granite mountain (standing 850 m above the surrounding planes). (Bottom Right panel) Horizontal map showing Granite mountain with mean wind and DH2 trajectories.
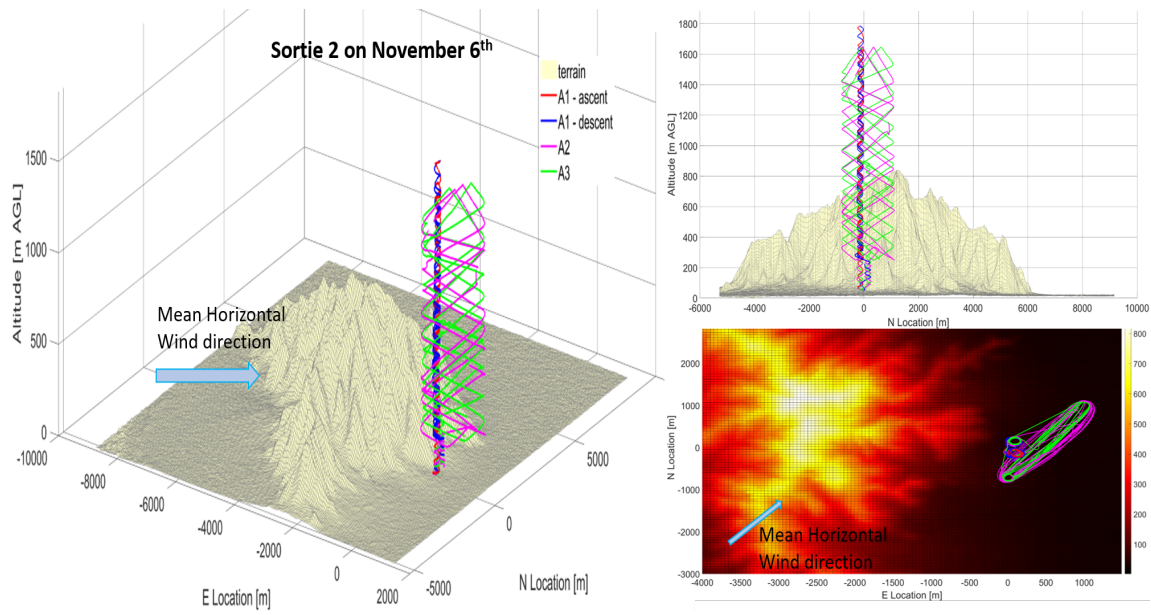
Figure 7. Trajectories of the vertically 'sounding' aircraft A1, and 'laterally' sounding aircraft A2 and A3 from Sortie 2 on 6 November 2017.
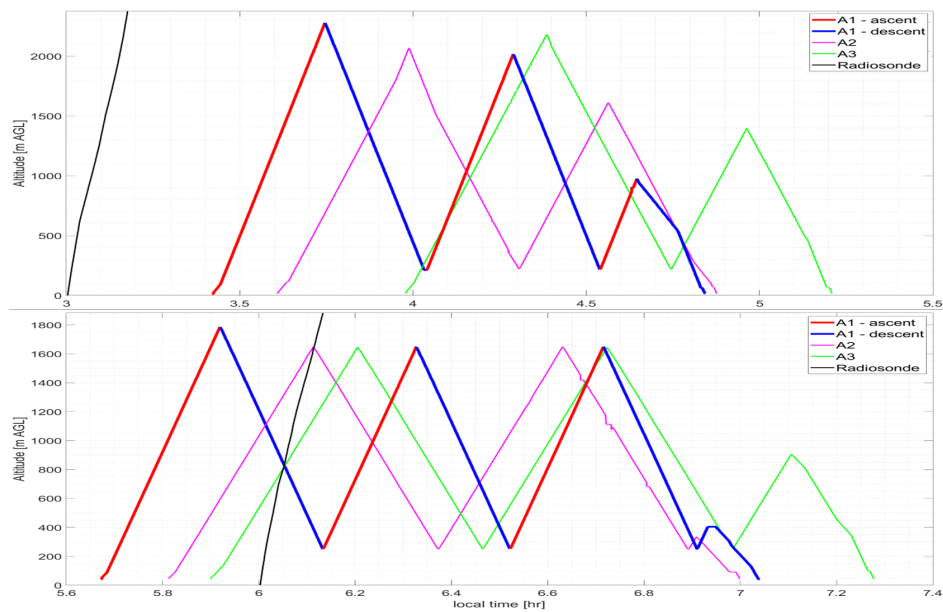
Figure 8. Timeseries (LT) showing altitude profiles for vertically sounding aircraft A1 (red - ascent; blue - descent), and laterally sounding aircraft A2 and A3 (magenta and green) co-ordinated with a radiosonde trajectory (black) for sorties 1 (top) and 2 (bottom) on 6 November 2017.

Sortie number	Date	Flight launch time (HH:MM) - LT	Flight launch site	Flight number	Flt. ceiling and Meas. strategy
S01	24-Oct-17	06:08	FS1	DH03 DH04	DH03 - spiral; ceiling - 1000 m DH04 - slant racetrack between 50 - 1100 m
S02	26-Oct-17	04:05	FS1	DH05	DH05 - spiral; ceiling - 1700 m
S03	26-Oct-17	05:53	FS1	DH06 DH07	DH07 - spiral; ceiling - 1300 m DH06 - slant racetrack between 300 - 1100 m
S04	28-Oct-17	02:55	FS1	DH08	DH08 - spiral; ceiling - 1800 m
S05	28-Oct-17	05:12	FS1	DH09 DH10	DH09 - spiral; ceiling - 2100 m DH10 - slant racetrack between 900 - 1100 m
S06	30-Oct-17	02:44	FS1	DH11 DH12 DH13	DH11 - spiral; ceiling - 2200 m DH12, DH13 - slant racetrack between 200 - 2100 m
S07	31-Oct-17	05:07	FS1	DH14 DH15	DH14 - spiral; ceiling - 2550 m DH15 - slant racetrack between 250 - 2550 m
S08	01-Nov-17	03:16	FS2	DH16 DH17	DH17 - spiral; ceiling - 3100 m DH16 - slant racetrack between 200 - 2700 m
S09	01-Nov-17	06:00	FS2	DH18 DH19	DH19 - spiral; ceiling - 1550 m DH18 - slant racetrack between 200 - 1550 m
S10	02-Nov-17	02:50	FS1	DH20 DH21	DH21 - spiral; ceiling - 2700 m DH20 - slant racetrack between 50 - 2700 m
S11	02-Nov-17	05:12	FS1	DH22 DH23	DH22, DH23 - slant racetrack between 50 - 2600 m

Sortie number	Date	Flight launch time (HH:MM)	Flight launch site	Flight number	Meas. strategy and target alt.
S12	02-Nov-17	06:57	FS1	DH24	DH24 - spiral; ceiling - 1600 m
S13	03-Nov-17	02:54	FS1	DH25 DH26	DH26 - spiral; ceiling - 3100 m DH25 - slant racetrack between 50 - 3100 m
S14	03-Nov-17	04:48	FS1	DH27 DH28	DH28 - spiral; ceiling - 3100 m DH27 - slant racetrack between 50 - 3100 m
S15	03-Nov-17	06:34	FS1	DH29 DH30	DH30 - spiral; ceiling - 3000 m DH29 - slant racetrack between 50 - 3000 m
S16	06-Nov-17	02:45	FS2	DH31 DH32 DH33	DH33 - spiral; ceiling - 2400 m DH31, DH31 - slant racetrack between 200 - 2200 m
S17	06-Nov-17	05:17	FS2	DH34 DH35 DH36	DH36 - spiral; ceiling - 1800 m DH34, DH35 - slant racetrack between 200 - 1600 m
S18	07-Nov-17	02:44	FS2	DH37 DH38	DH38 - spiral; ceiling - 2400 m DH37 - slant racetrack between 900 - 2300 m
S19	07-Nov-17	04:37	FS2	DH39 DH40	DH40 - spiral; ceiling - 2000 m DH39 - slant racetrack between 800 - 1500 m
S20	07-Nov-17	06:24	FS2	DH41	DH41 - spiral; ceiling - 2100 m
S21	09-Nov-17	03:02	FS1	DH42	DH42 - spiral; ceiling - 1800 m
S22	09-Nov-17	05:59	FS1	DH43 DH44 DH45	DH45 - spiral; ceiling - 1600 m DH43, DH44 - slant racetrack between 100 - 600 m

Sortie number	Date	Flight launch time (HH:MM)	Flight launch site	Flight number	Meas. strategy and target alt.
S23	10-Nov-17	02:53	FS2	DH46 DH47 DH48	DH48 - spiral; ceiling - 2600 m DH46, DH47 - slant racetrack between 200 - 2500 m
S24	10-Nov-17	05:12	FS2	DH49 DH50 DH51	DH51 - spiral; ceiling - 2600 m DH49, DH50 - slant racetrack between 500 - 2500 m
S25	11-Nov-17	02:47	FS2	DH52 DH53 DH54	DH54 - spiral; ceiling - 3000 m DH52, DH53 - slant racetrack between 200 - 2800 m
S26	11-Nov-17	04:42	FS2	DH55 DH56	DH56 - spiral; ceiling - 950 m DH55 - slant racetrack between 150 - 900 m
S27	13-Nov-17	02:53	FS2	DH57 DH58 DH59	DH59 - spiral; ceiling - 3100 m DH57, DH58 - slant racetrack between 200 - 3100 m
S28	13-Nov-17	06:22	FS2	DH60 DH61 DH62	DH62 - spiral; ceiling - 3100 m DH60, DH61 - slant racetrack between 1700 - 2800 m
S29	14-Nov-17	02:53	FS1	DH63 DH64 DH65	DH65 - spiral; ceiling - 2200 m DH63, DH64 - slant racetrack between 100 - 1400 m
S30	14-Nov-17	05:08	FS1	DH66 DH67	DH67 - spiral; ceiling - 2400 m DH66 - slant racetrack between 800 - 1400 m
S31	15-Nov-17	02:44	FS2	DH68 DH69 DH70	DH70 - spiral; ceiling - 3100 m DH68, DH69 - slant racetrack between 1100 - 2400 m

Table 3. List of DH2 UAS sorties deployed during IDEAL observation program. The launch date, site, time (HH:MM - 00-24 hour), flight ceiling and observation strategy for aircraft in each sortie are presented.

4 Data Processing and Preliminary Results

The sensor data sampled from DH2 observation flights is telemetered to the ground station for real-time display and also written periodically on-board a micro SD card as binary data in $4\,\mathrm{KB}$ packets. An extensive suite of programs has been developed using MATLAB to carefully calibrate the raw DH2 sensor measurements and compute meaningful scientific data products during
260 post-flight data analysis. The DH2 instrument configuration, outlined in Section 2.1, consists of a custom Pitot static tube fitted to a pressure sensor, a hotwire anemometer, and a coldwire thermometer that provide airspeed (in $\mathrm{ms^{-1}}$) and temperature (in K) at a high-cadence of $800\,\mathrm{Hz}$ are used to estimate ϵ and C_T^2. The Pitot derived airspeed data along with the GPS velocity and aircraft attitude information provided by the DH2 autopilot standard sensor suite are used to estimate the mean horizontal wind vector. A novel wind estimation algorithm, improving the estimation procedure described by Lawrence and Balsley (2013),
265 was developed as part of the lead author's doctoral thesis (Doddi, 2021). This novel wind estimation algorithm was to the DH2 measurements from the IDEAL program to obtain estimates of mean horizontal wind vector at a cadence of $1\,\mathrm{Hz}$ and accurate up to $0.05\,\mathrm{ms^{-1}}$.
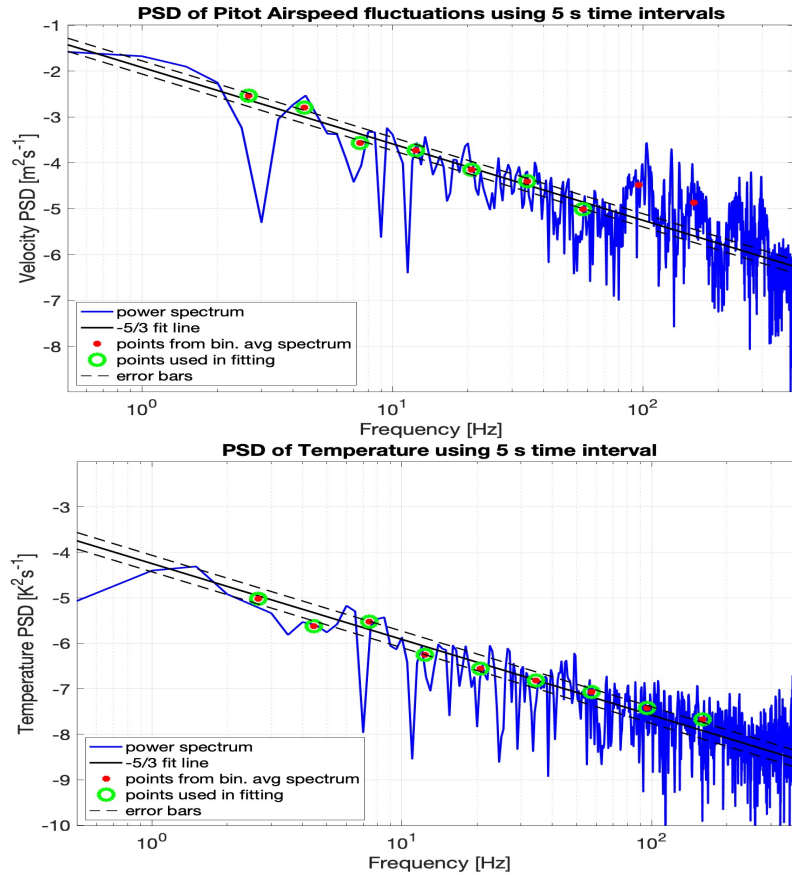
Figure 9. PSD of Pitot derived airspeed (top tile) and coldwire derived temperature (bottom tile) plotted against sampling frequency. The $f^{-5/3}$ fit line (solid black) along with the fit variance (dashed black) are shown.

Following the estimation procedures described by Frehlich et al. (2003) and Luce et al. the turbulence parameters of ϵ and C_T^2 are determined by applying spectral analysis to high-cadence airspeed and temperature measurements. The power spectral density (PSD) of high-cadence airspeed (and temperature) is computed using non-overlapping 5 s time intervals. The measured PSD of airspeed (and temperature) are fit to the model spectra proposed by Tatarskii (1971) using a novel spectral fitting algorithm to then compute ϵ (and C_T^2). The spectral analysis and fitting procedures employed to analyze DH2 measurements during the IDEAL program are described in detail in the lead author's doctoral thesis document Doddi (2021). Figure 9 visualizes the spectral analysis algorithm through example PSD of pitot derived airspeed (top tile) and coldwire derived temperature (bottom tile) plotted against sampling frequency on a log10 scale. The raw PSD (solid blue) is binned into 9 equally spaced frequency bins between $2-200$ Hz and averaged (red pucks). The bin-averaged PSD points are fits to a $f^{-5/3}$ slope line omitting the spectral artifacts (e.g. 95 and 105 Hz points in the top panel) to determine the mean and variance of the spectral fit. This is used to provide estimates (including the variance) of ϵ and C_T^2 for each 5 s time interval.

In addition to the 2D mean wind vector, ϵ and C_T^2 estimates the parameters generally used to define the static and dynamic stability of the atmosphere are also computed. First, the coldwire temperature, 2D mean wind vector, and calibrated pressure altitude are filtered using a zero-phase distortion digital filter and resampled to 10 Hz. Subsequently, the potential temperature (θ), Brunt-Vaisala frequency (N), vertical shear (dU/dz), and the gradient Richardson number (Ri) are calculated. Figures 10, 11, 12, 13 show altitude profiles of the DH2 measured and estimated parameters for the vertically sounding aircraft (A1 in Figures 6 and 7) from two sorties deployed at FS1 (see Figure 1) on 6 November 2017. The ascent (solid red line) and descent (solid blue line) flight legs are offset by a fixed scale to visualize the evolution of various flow features. Also depicted in these figures are the profiles obtained from radiosonde deployments at FS2 co-ordinated with the DH2 sorties.
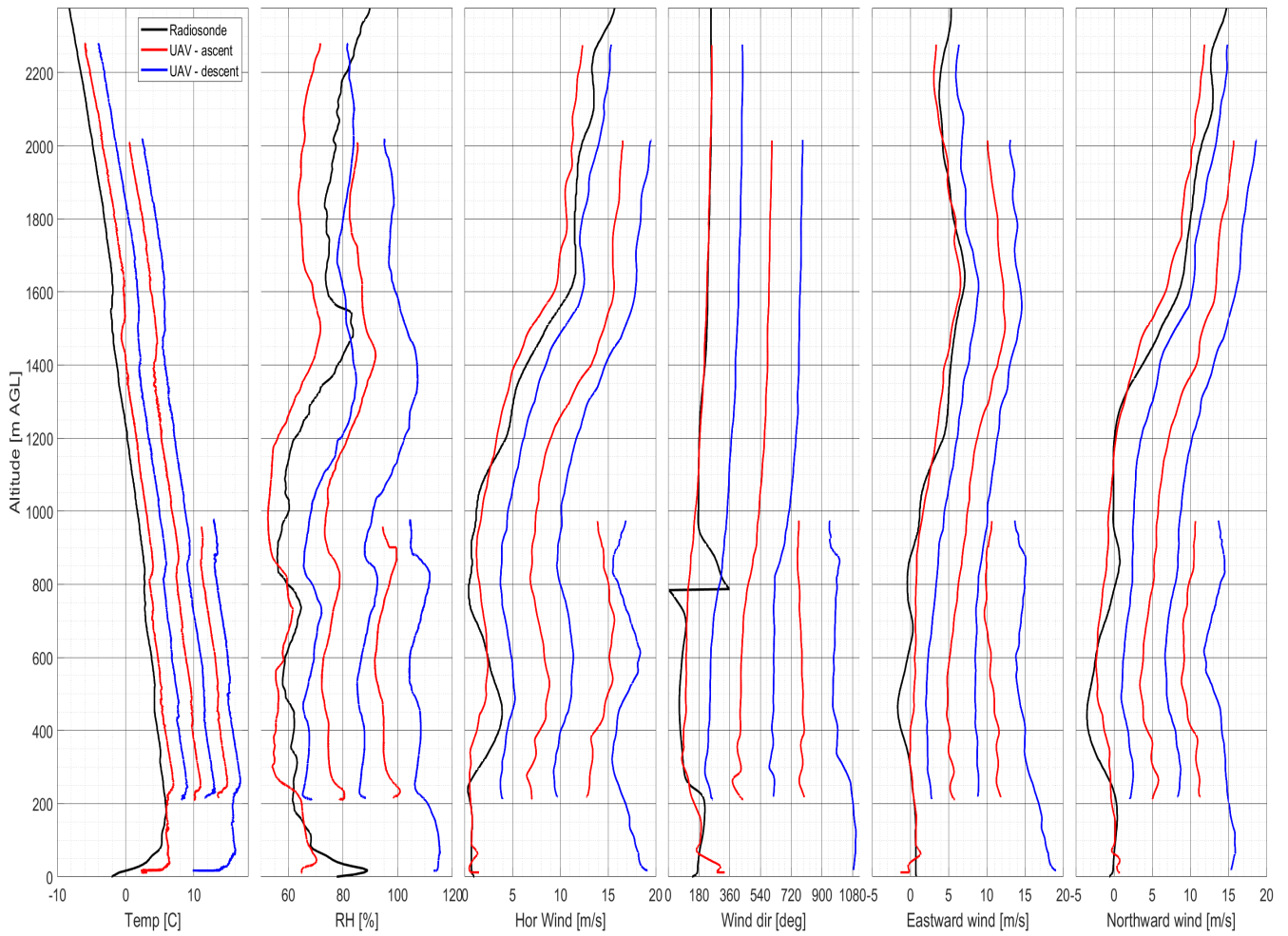
Figure 10. Vertical profiles (offset for clarity) of 800 Hz temperature (offset: 2 C), 100 Hz humidity (offset: 10%), 10 Hz horizontal wind speed (offset: 3 ms^{-1}) and direction (offset: 180°), eastward and northward winds (offset: 3 ms^{-1}) from the vertical sounding aircraft in S1 on 6 November 2017. Red (blue) lines indicate ascending (descending) flight legs.
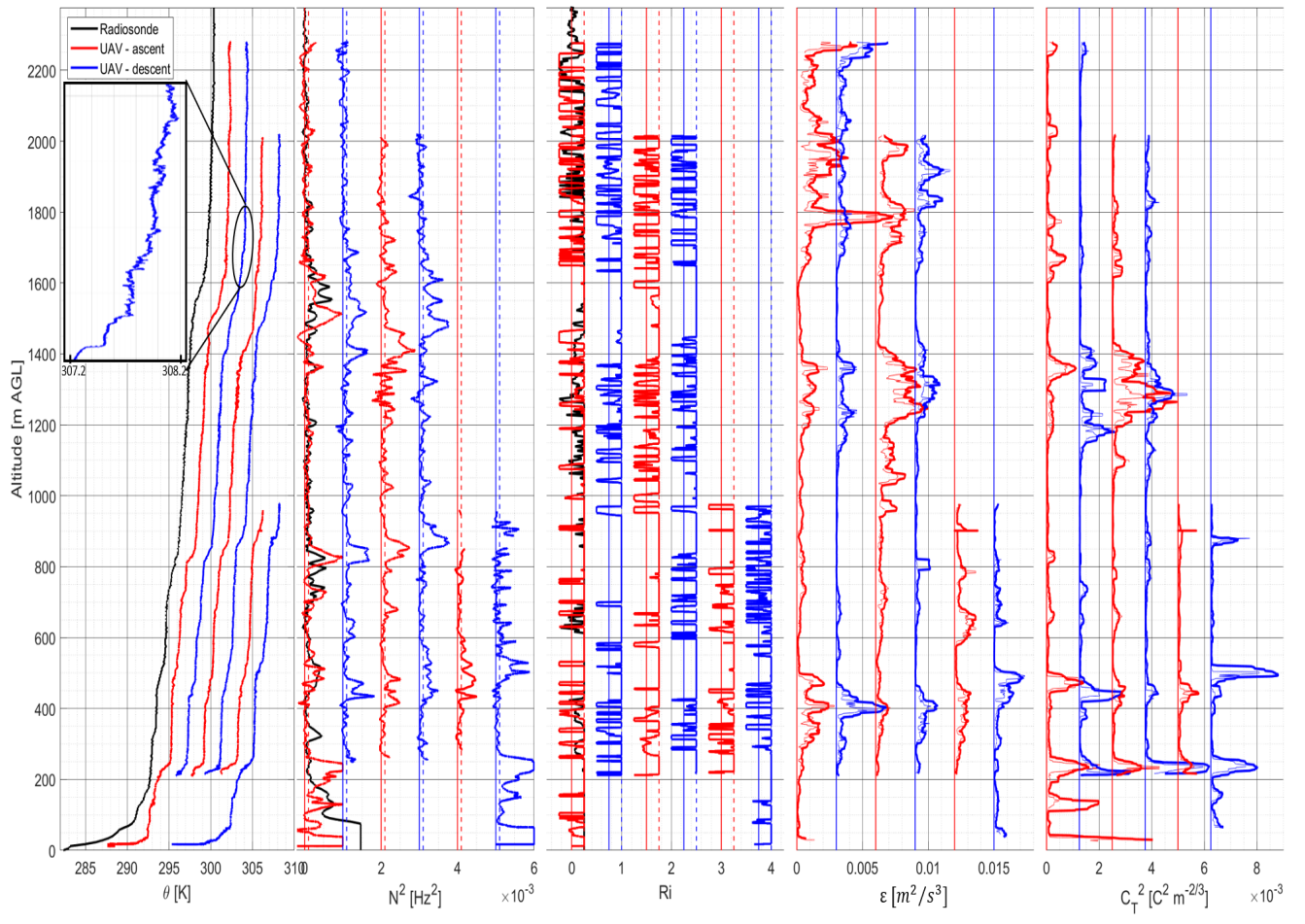
Figure 11. Vertical profiles (offset for clarity) of 800 Hz θ (offset: 2 K), 10 Hz N (offset: 10^{-3} s^{-2}, dash line: $N^2 = 10^{-4} s^{-2}$ s^{-2}), 10 Hz Ri (offset: 0.75, dash line: $Ri = 0.25$), ϵ (offset: 3×10^{-3} m^{2}s^3) and C_T^2 (offset: 1.25×10^{-3} C^{2}m$^{-2/3}$) estimated using 5 s time records from the vertical sounding aircraft in S1 on 6 November 2017.
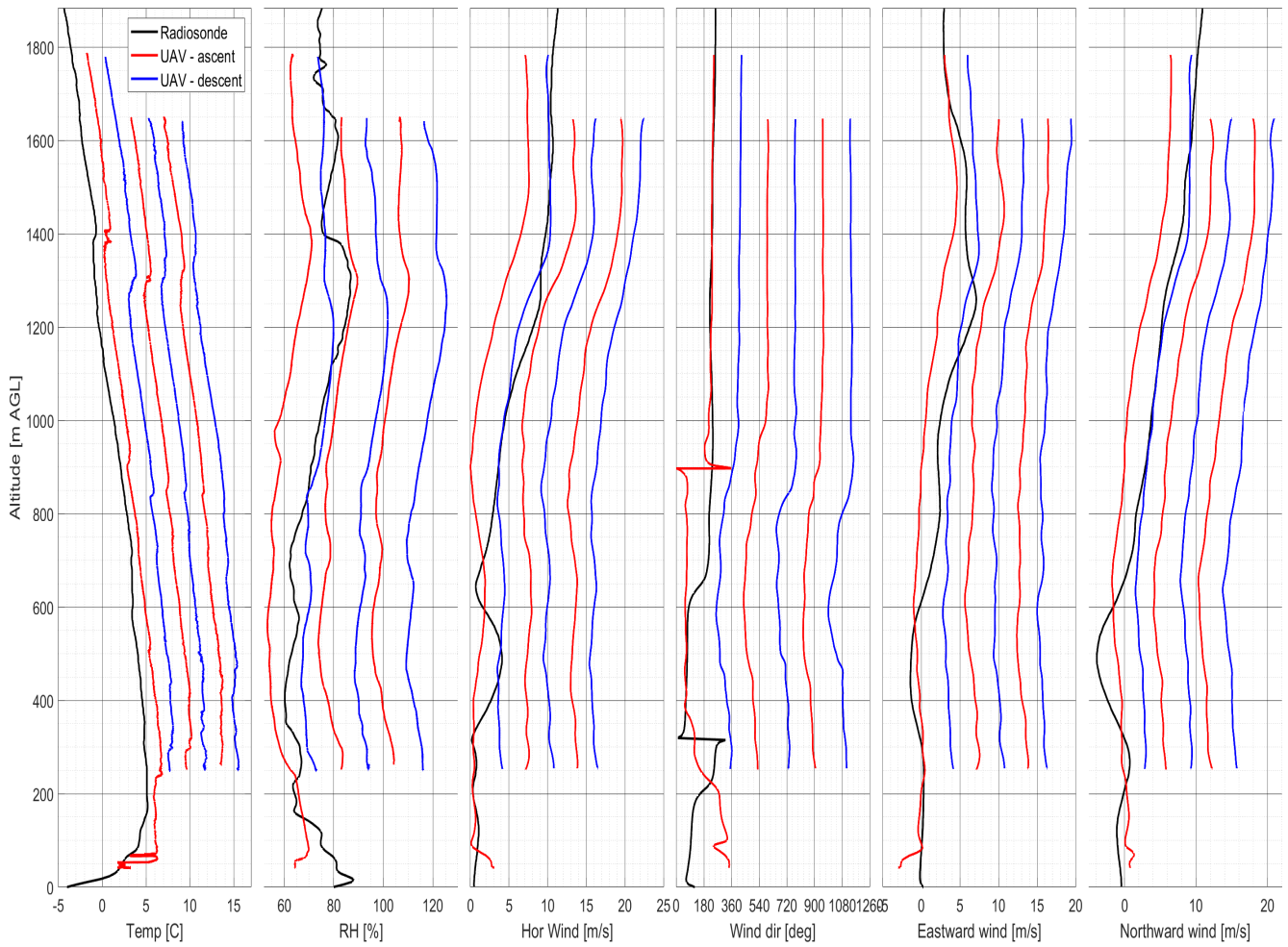
Figure 12. Vertical profiles of Temperature, Humidity, horizontal wind speed and direction, Eastward and Northward Winds from the vertically sounding aircraft in S2 on 6 November 2017.
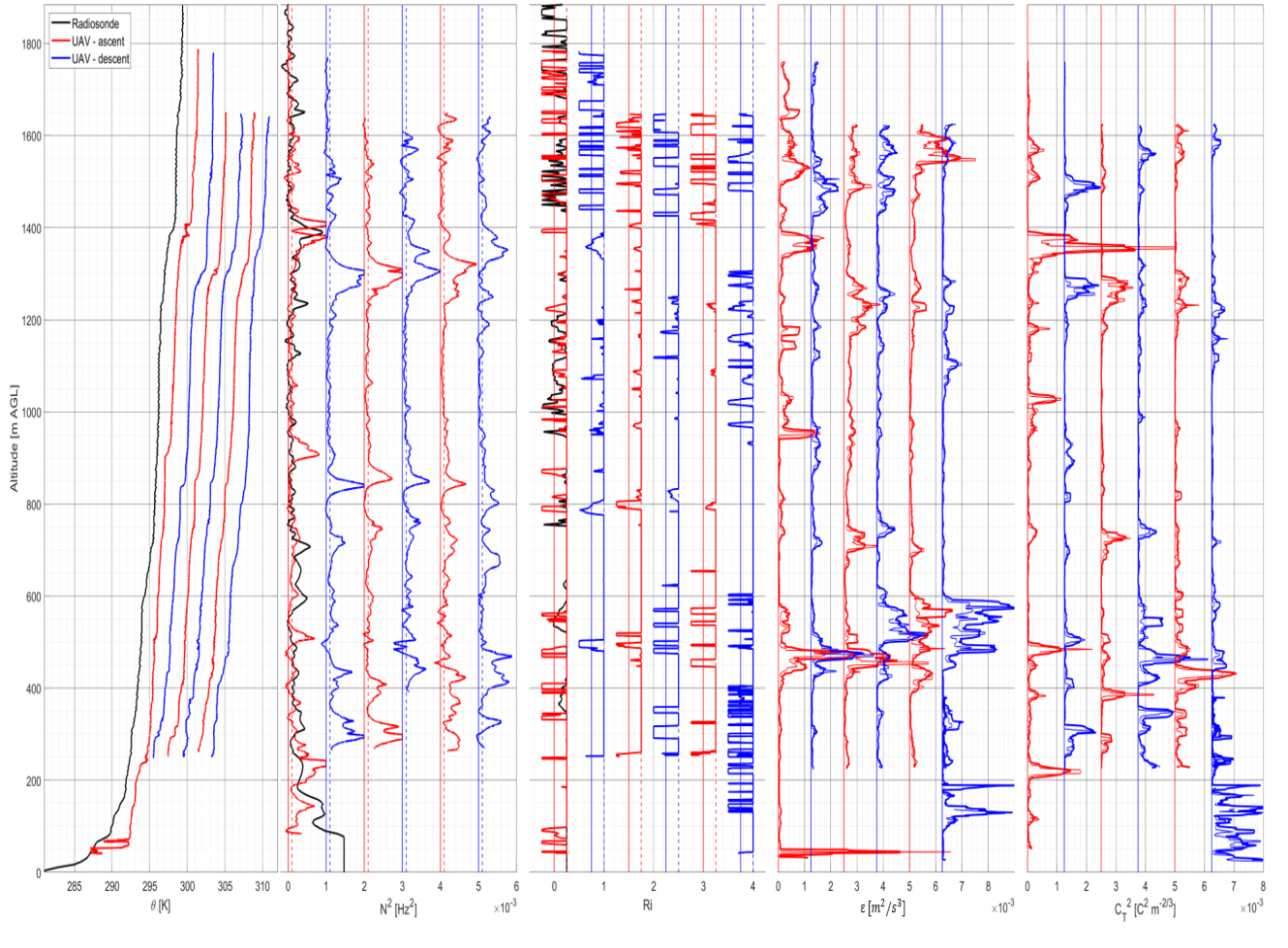
Figure 13. Vertical profiles of Potential temperature, Buoyancy frequency, Gradient Richardson Number, TKE dissipation rate (offset: 1.25×10^{-3} m^{2}s^{-3}), and temperature structure function from the vertically sounding aircraft in S2 on 6 November 2017.

Following the criterion described by Muschinski and Wode (1998) and Dalaudier et al. (1994), temperature gradients on the order of 17Γ (Γ - adiabatic lapse rate) were used to identify the edges of stability sheets. A total of 58 individual stable sheet structures roughly 25 to 50 m deep from DH2 UAS measurements of high-resolution temperature data. Stability ducts, consisting of large N^2 sheets constraining weakly stable and weakly turbulent layers as deep as 400 m, were frequently prevalent. Such structures, often persisting up to five hours under very stable conditions, were commonly observed at the peak altitude of Granite mountain (850 to 900 m AGL). Altitude undulations in persisting stable structures during strong (8 to 10 ms^{-1}) eastward-wind forcing over Granite mountain suggest the presence of mountain waves. Temperature gradients as steep as 0.18 Km^{-1} or $\sim 18\Gamma$ (with tropospheric dry adiabatic lapse rate $\Gamma \sim 9.8 \times 10^{-3}$ Km^{-1}) were typically observed across most sheets (see enlarged inset on Figure 11).

The sorties presented in Figures 10, 11, 12 and 13 show a stable nocturnal boundary layer extended to 200 m, and capped by an inversion layer at these times. Eastward wind aloft up to 12 ms^{-1} was observed. A strong speed shear developed between 1200 and 1600 m AGL. The background atmospheric column was near-neutrally stable ($N^2 = 10^{-5}s^{-2}$). The DH2 observed an undulating sheet in the measurements of temperature and humidity at 800 m and another sheet formation at 1500 m. An intermittent patch of weak turbulence, 200 m deep, was observed between 1400 and 1600 m. Subsequent vertical profiles of ϵ and C_T^2 in Figures 11 (from S1 at 03 LT) and 13 (from S2 at 05 LT) exhibit signs of diminishing turbulence likely leading to re-laminarization enabling formation of a steep temperature gradient that is characteristic of a highly stable sheet. The extinction of turbulence is apparent in the abrupt reduction of ϵ just below 1400 m from the first ascent to the first descent in Figure 13. The confined elevation of C_T^2 immediately below 1400 m in Figure 13 further supports this conclusion.

Figures 14 and 15 show profiles of the measured and estimated parameters from hourly radiosonde soundings monitoring the atmospheric column at FS2 (9.5 km downstream of FS1) on 6 November 2017. The θ and RH profiles from these periodic soundings suggest that the two sheets observed by DH2 at FS1, shown in Figures 10 and 11 (at 800 m and 1300 m), are highly localized and likely decay as they advect. The undulating motion exhibited by the sheets suggests weak wave activity in the leeward side of Granite mountain as a consequence of strong eastward wind forcing. Preliminarily, this case seems to align well with the analysis presented in Balsley et al. (2018) implying that S&L structures are maintained by GW-FS interactions.

A shallow nocturnal boundary layer (200 m deep), recurring sheet activity at the mountain top (850 m) and aloft (1450 - 1600 m) separated by deep, intermittent turbulent layers (600 - 800 m deep) was the general theme underlying the observations at FS1. Escalation of shear at altitudes coincidental with the undulating sheet pairs probably destabilized the sheets causing them to decay, and sustain turbulence inside the layers.
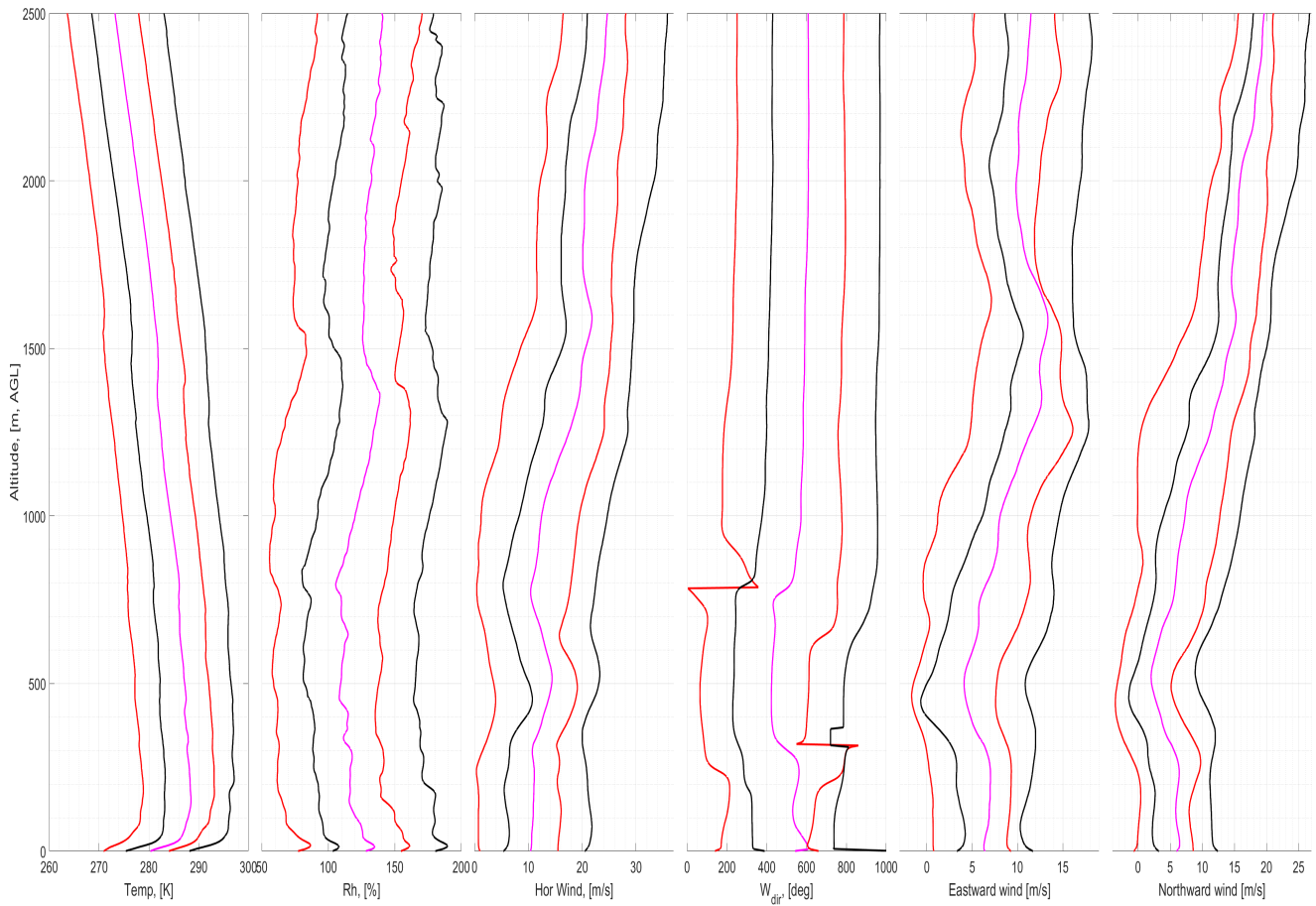
Figure 14. Height plots of Temperature (offset: 5 C), Humidity (offset: 25%), horizontal wind speed (offset: 5 ms^{-1}) and direction (offset: 1800 °), Eastward and Northward Winds (offset: 3 ms^{-1}) from five hourly radiosonde launches between 03:00 and 07:00 LT on 6 November 2017.
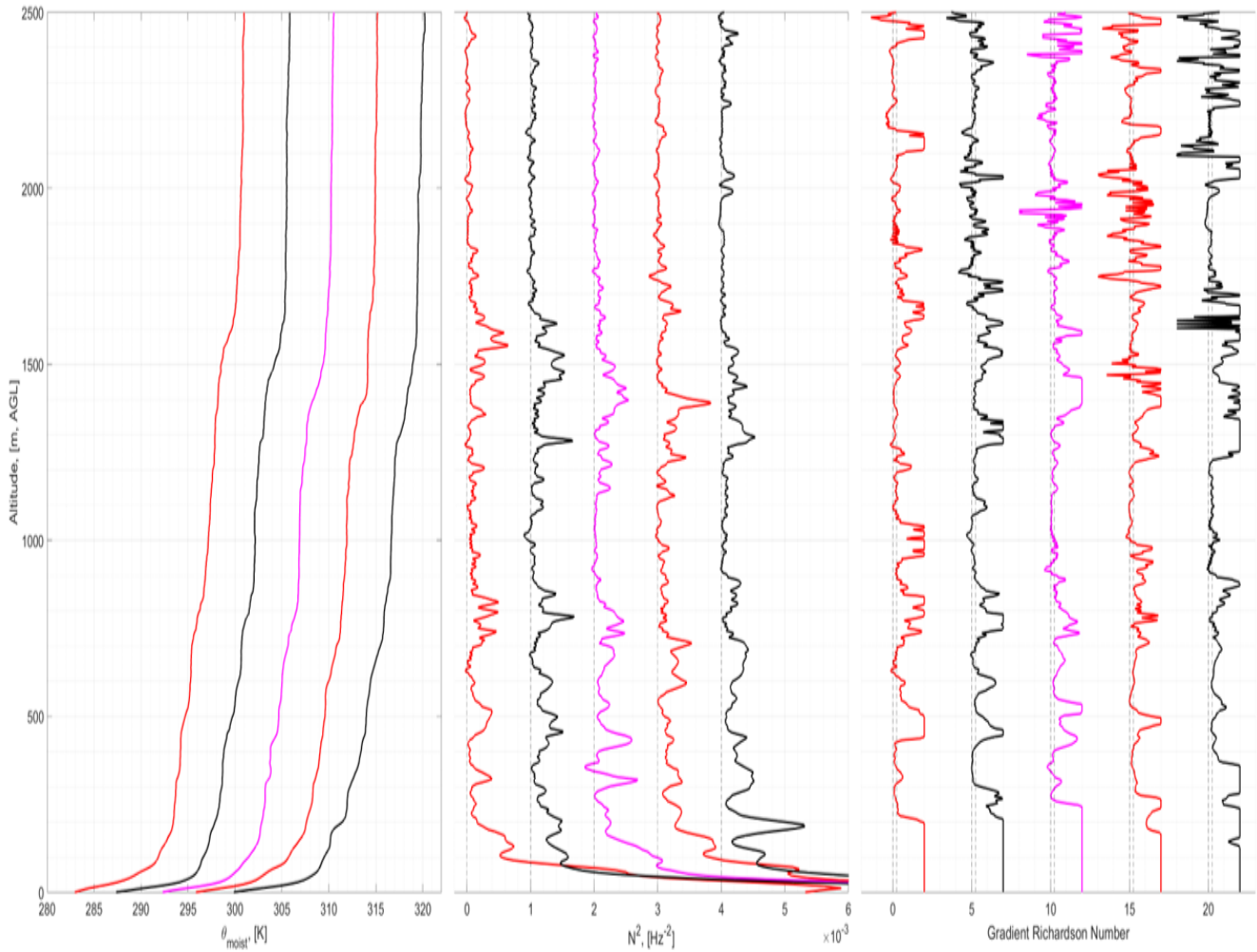
Figure 15. Height plots of Potential temperature (offset: 5 K), Buoyancy Frequency (offset: 10^{-3} s^{-2}) and Gradient Richardson Number (offset: 5, dash line: Ri = 0.25) estimates from five hourly radiosonde launches between 03:00 and 07:00 LT on 6 November 2017.

315 Preliminary analysis of the measurements made by laterally sampling aircraft (A2 and A3 aircraft from each sortie) is underway. Figures 16 and 17 depict 2D scatter plots T/RH, θ, Pitot and hotwire derived ϵ, and coldwire derived C_T^2 as a function of altitude and longitude for the laterally sampling A3 aircraft from S1 on 6 November 2017. The Figures 18, and 19 show timeseries of the scatter plots in Figures 16, and 17. The uniform T/RH and θ along the lateral extent of the sheets (1.5 km) between 1200 and 1400 m in Figures 16 and 17 suggest that this shallow layer exhibits uniform temperature and

320 stratification across the lateral measurement extent suggesting that the layer spans a few kilometers laterally. However, the lateral variability in the estimates of ϵ and C_T^2 suggests localized, weak, and intermittent turbulence patches within the mixed layer.

The slanted lateral sampling strategy employed by A2 (and A3) aids in decoupling the spatial and temporal variations in the measurements of these unsteady, localized, and potentially advecting turbulence patches and provides insights on the intermittency and evolution of small-scale weak turbulence within the shallow mixed layers. A rigorous analysis of DH2 data products is expected to provide further insights on the lateral structure and variability of S&L, but limited information on the formation mechanism. However, DH2 measurements provide qualitative information on the background structure and forcing conditions invaluable for initializing and validating the qualitative results of future DNS of such multiscale turbulence dynamics in the free atmosphere.
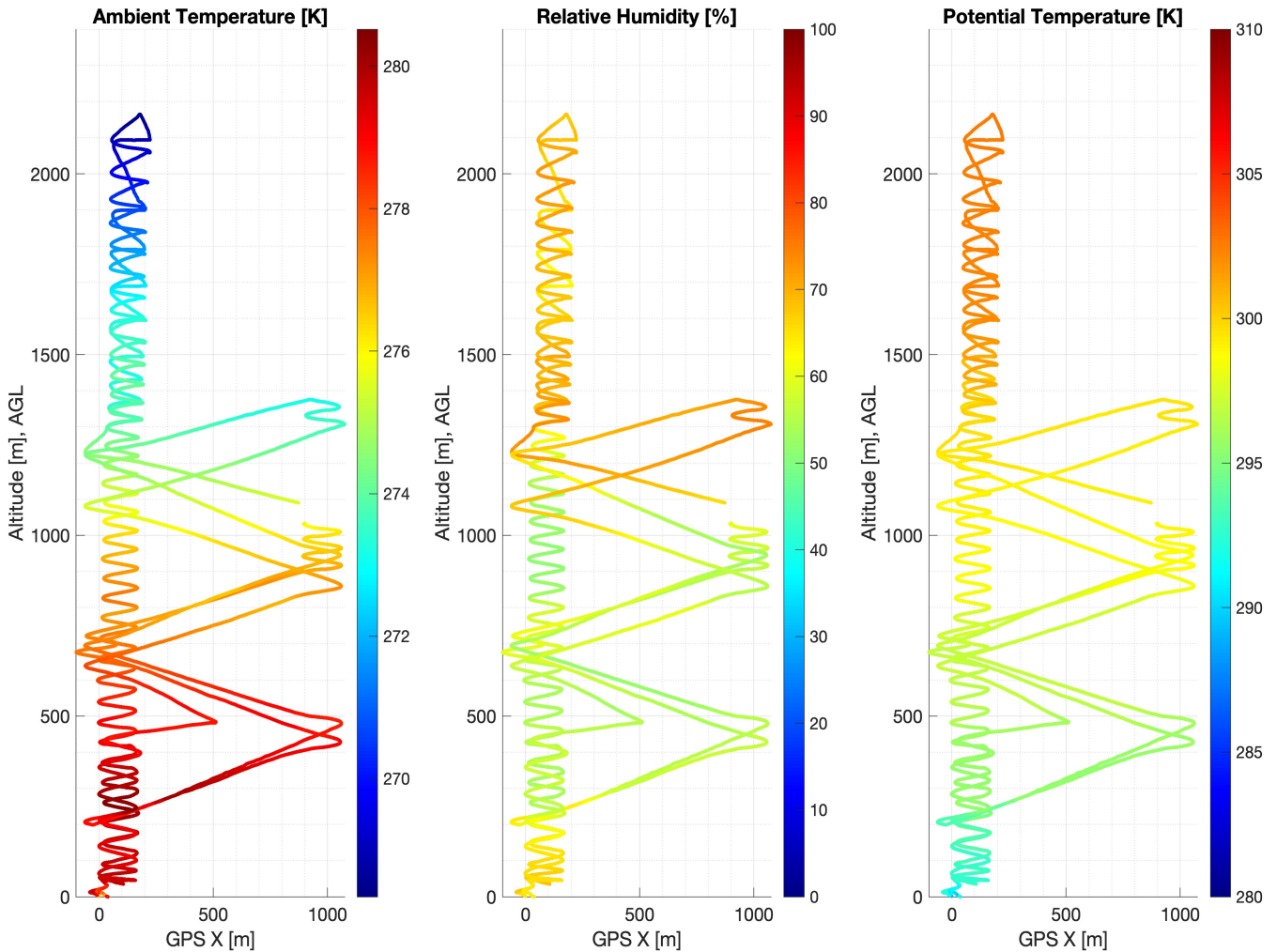
Figure 16. Scatter plot of T/RH, and θ plotted as a function of altitude and longitude for the lateral sounding DH2 aircraft from the first sortie (S1) on 6 November 2017.
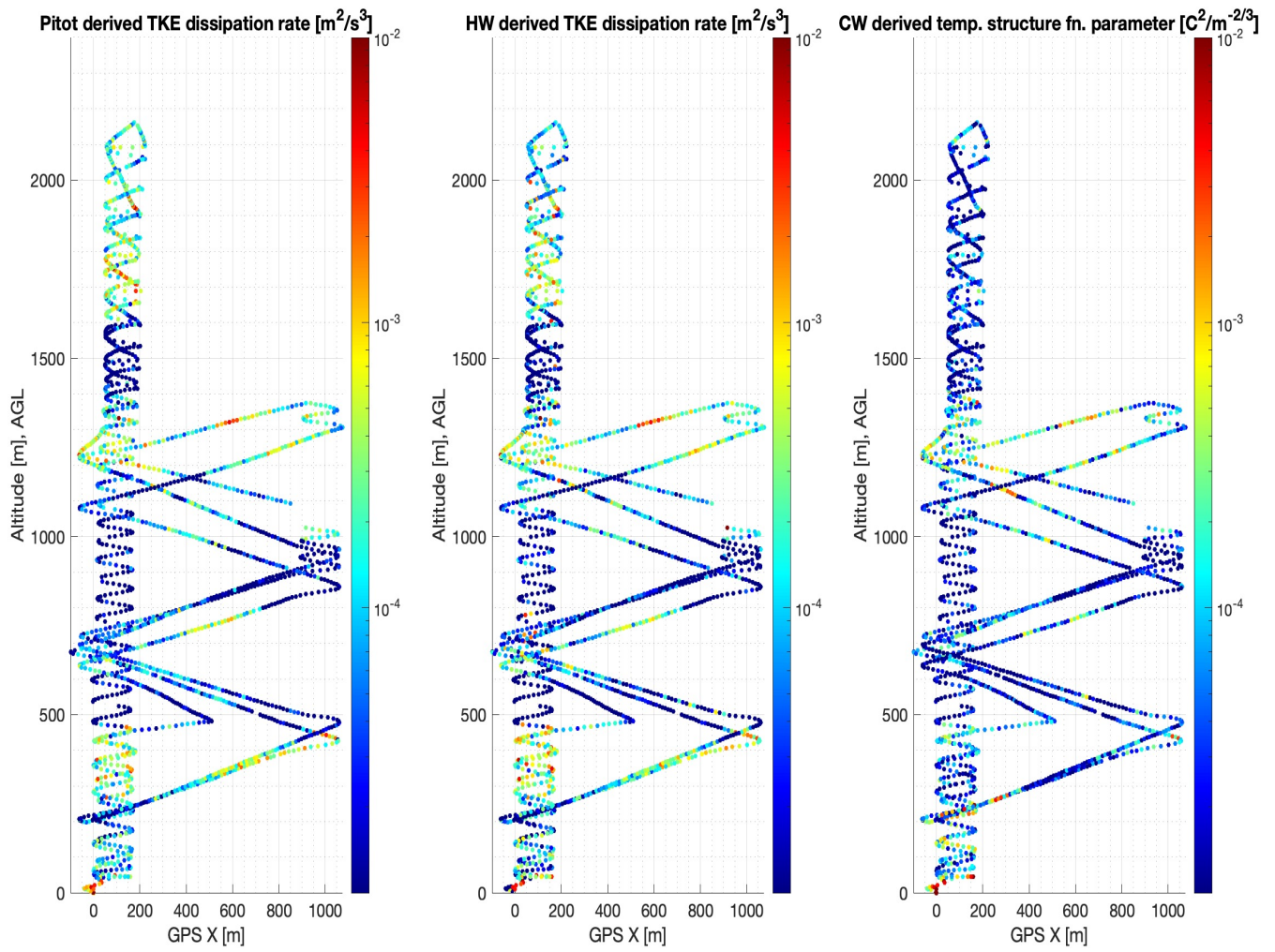
Figure 17. Scatter plot of Pitot and hotwire derived ϵ and coldwire derived c_T^2 plotted as a function of altitude and longitude for the lateral sounding DH2 aircraft from the first sortie (S1) on 6 November 2017.
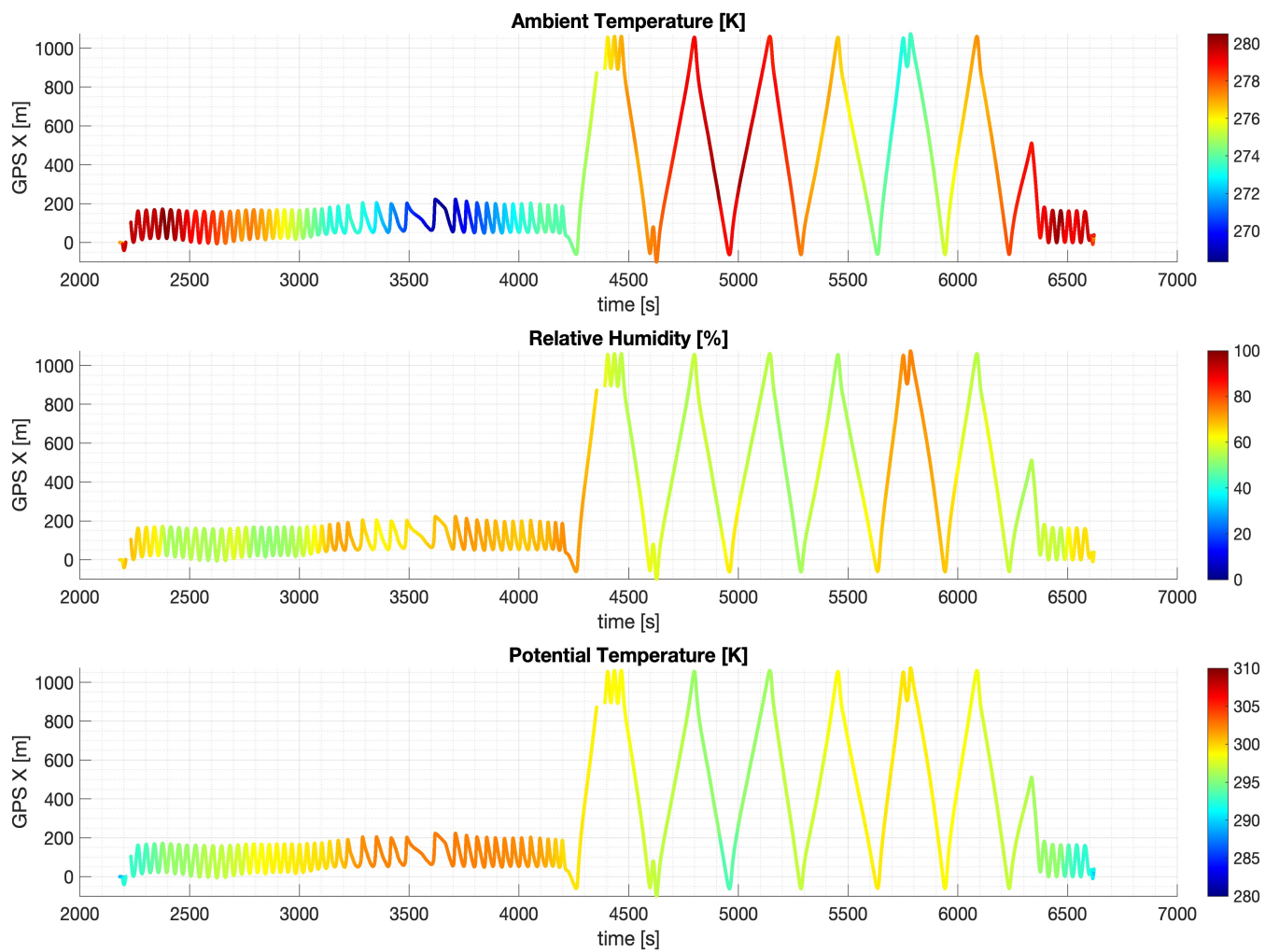
Figure 18. Timeseries scatter plot of T/RH, and θ plotted as a function of longitude for the lateral sounding DH2 aircraft from the first sortie (S1) on 6 November 2017.
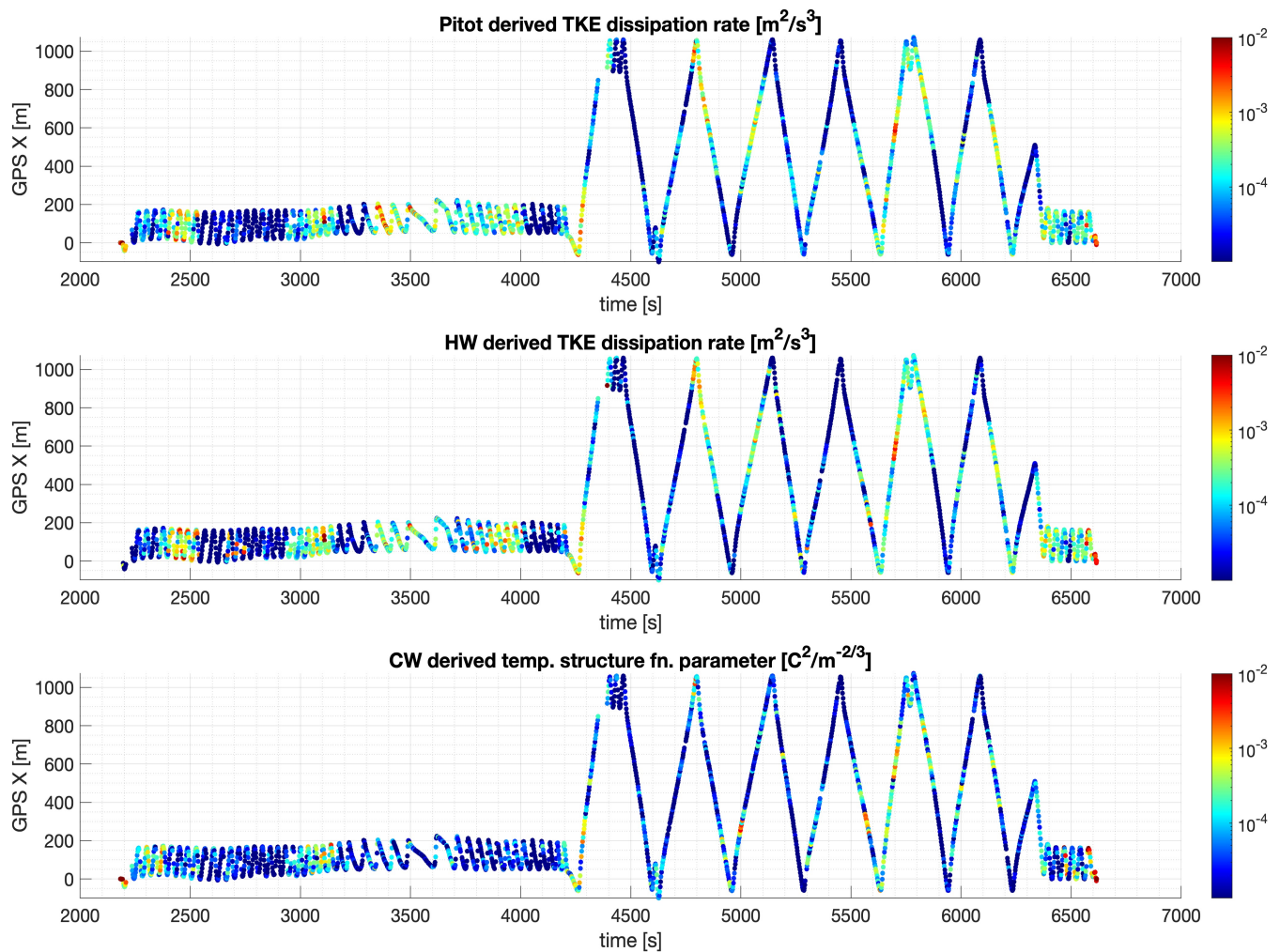
Figure 19. Timeseries scatter plot of Pitot and hotwire derived ϵ and coldwire derived c_T^2 plotted as a function of longitude for the lateral sounding DH2 aircraft from the first sortie (S1) on 6 November 2017.

330 The summary plots as portrayed in all the figures presented in this section along with other preliminary analysis data, relevant flight notes and flight metadata for each DH2 UAS sortie (and hourly radiosonde deployments) are available for download through the IDEAL preliminary analysis website hosted by the University of Colorado at https://www.colorado.edu/p129765c7060/home. The observational data from sUAS, ISS soundings and 915 MHz radar wind profiles, DPG 449 MHz radar wind profiles, SAMS, mini SAMS and ancillary data are available for download on request at https://www.eol.ucar.edu/

335 field_projects/ideal in standard binary formats (.netcdf and .mat). Documents describing processing and quality control for all the platforms along with the metadata files are made available with the datasets. The suite of scripts developed to process and analyze DH2 and radiosonde measured data during the IDEAL observation program are maintained on a private GitHub repository and will be shared on request by correspondence with the lead author.

5 Conclusions and Future work

340 The IDEAL observational and modeling program was conceived to further our understanding of the structure and formation of multiscale S&L dynamics by extensively observing using high-resolution UAS and coordinated radiosonde instruments. The S&L structures are ubiquitous in the nocturnal boundary layer under relatively quiescent conditions, often extend to higher altitudes in the lower troposphere, and have parallels extending to much higher altitudes at larger spatial scales. IDEAL program was motivated by multiple previous radar observations and high-resolution in-situ profiling measurements revealing

345 the ubiquitous occurrence of S&L structures and initial high-resolution modeling of KHI MSD demonstrating the emergence of S&L dynamics from idealized initial conditions. In this article, we discussed the DH2 UAS instrumentation and observation strategy employed at DPG in Utah with guidance from daily local WRF weather forecasts, ISS wind profiler radar and hourly radiosonde profiles. The UAS sorties deployed during IDEAL were unique because they were the first to employ DH2 UAS for coordinated, multi-UAS sorties performing coincident, but diverse, flight profiles in a common volume.

350 The vertical profiling aircraft, deployed first during each sortie, surveyed the atmospheric column and relayed in real-time to the ground station. This information was used to guide and steer the lateral profiling aircraft in each sortie. This seminal multi-aircraft sampling strategy enabled diverse observations of S&L dynamics that aided in characterizing numerous unsteady, advecting, weak and intermittent turbulence layers in the free troposphere (up to $3\,\mathrm{km}$). Preliminary analysis of lateral profiling aircraft measurements suggest weak (strong), intermittent (persisting), and highly localized (spanning a km) turbulent layers

355 at $850\,\mathrm{m}$ and $1500\,\mathrm{m}$ in the leeward side of Granite Mountain. The initial assessment of data from lateral sounding aircraft on 6 November 2017 presented in Section 4 were found to be qualitatively consistent with the description of the S&L structures described by Tjernström et al. (2009) and Balsley et al. (2018). Although preliminary analysis of lateral profiling DH2 UAS provided valuable insights on the morphology and evolution of shallow turbulent layers, a detailed analysis and interpretation of this data is hampered due to the complexity in distinguishing the spatial and temporal variability in the data with steady,

360 localized and advecting turbulence patches.

The IDEAL observations have characterized multiple events that we anticipate will provide guidance for diverse further modeling studies. Important among these will be additional modeling of KHI T&K dynamics (see Section 1) induced by MSD at larger scales. These dynamics may be especially beneficial, given their recent discovery in atmospheric observations and initial DNS modeling results suggesting that they may have important implications for mixing and induced larger-scale

365 motions in the atmosphere, oceans, and other stratified and sheared fluids.

Acknowledgements. The IDEAL field program and modeling efforts were supported by the US National Science Foundation (NSF) grants AGS-1632772 and AGS-1632829, with related modeling efforts supported by AGS-2032678 and AGS 1758293. The authors would like to acknowledge the efforts of Tyler Mixa and Kam Wan of GATS for their assistance in the performance of DH2 sUAS measurements during the field program. Isabel Suhr at NCAR EOL assisted William Brown with radiosonde launch. The authors would also like to acknowledge

370 the DPG Meteorology division for providing detailed weather forecasting, reports, and briefings.

Author contributions.

DF conceived the joint IDEAL measurement and modeling program and guided the initial DNS modeling components with assistance from TL and LW at GATS. DL developed the DH2 sUAS vehicles and AD assisted in developing and testing the sensing systems. DL led the DH2 portion of the field campaign and AD assisted in DH2 deployment. AD and DL carried out the preliminary DH2 data analyses. WB led the ISS siting, operations, and data handling activities, and DZ hosted the campaign at DPG, including coordination of daily weather briefings. DF and LK provided (remote) science guidance during the campaign.

Competing interests.

The authors have no competing interests regarding this work.

References

380 Alaoui-Sosse, S., Durand, P., Medina, P., Pastor, P., Lothon, M., and Cernov, I.: OVLI-TA: An Unmanned Aerial System for Measuring Profiles and Turbulence in the Atmospheric Boundary Layer, https://doi.org/10.3390/s19030581, 2019.

Altstädter, B., Platis, A., Wehner, B., Scholtz, A., Wildmann, N., Hermann, M., Käthner, R., Baars, H., Bange, J., and Lampert, A.: ALADINA – an unmanned research aircraft for observing vertical and horizontal distributions of ultrafine particles within the atmospheric boundary layer, Atmos. Meas. Tech., 8, 1627–1639, https://doi.org/10.5194/amt-8-1627-2015, https://www.atmos-meas-tech.net/8/1627/2015/https:

385 //www.atmos-meas-tech.net/8/1627/2015/amt-8-1627-2015.pdf, 2015.

Balsley, B. B., Frehlich, R. G., Jensen, M. L., Meillier, Y., and Muschinski, A.: Extreme Gradients in the Nocturnal Boundary Layer: Structure, Evolution, and Potential Causes, Journal of the Atmospheric Sciences, 60, 2496–2508, https://doi.org/10.1175/1520-0469(2003)060<2496:EGITNB>2.0.CO;2, https://doi.org/10.1175/1520-0469(2003)060%3C2496:EGITNB%3E2.0.COhttp://0.0.0.2, 2003.

390 Balsley, B. B., Frehlich, R. G., Jensen, M. L., and Meillier, Y.: High-Resolution In Situ Profiling through the Stable Boundary Layer: Examination of the SBL Top in Terms of Minimum Shear, Maximum Stratification, and Turbulence Decrease, Journal of the Atmospheric Sciences, 63, 1291–1307, https://doi.org/10.1175/JAS3671.1, https://doi.org/10.1175/JAS3671.1, 2006.

Balsley, B. B., Lawrence, D. A., Woodman, R. F., Fritts, D. C., Balsley, B. B., Lawrence, D. A., and Woodman, R. F.: Fine-Scale Characteristics of Temperature, Wind, and Turbulence in the Lower Atmosphere (0–1,300 m) Over the South Peruvian Coast, Boundary-Layer Meteorology, 147, 165–178, https://doi.org/10.1007/s10546-012-9774-x, https://link.springer.com/article/10.1007/s10546-012-9774-xhttps:

395 //doi.org/10.1007/s10546-012-9774-x, 2013.

Balsley, B. B., Lawrence, D. A., Fritts, D. C., Wang, L., Wan, K., and Werne, J.: Fine Structure, Instabilities, and Turbulence in the Lower Atmosphere: High-Resolution In Situ Slant-Path Measurements with the DataHawk UAV and Comparisons with Numerical Modeling, Journal of Atmospheric and Oceanic Technology, 35, 619–642, https://doi.org/10.1175/JTECH-D-16-0037.1, http://journals.ametsoc.org/

400 doi/10.1175/JTECH-D-16-0037.1, 2018.

Barat, J.: SOME CHARACTERISTICS OF CLEAR-AIR TURBULENCE IN THE MIDDLE STRATOSPHERE., Journal of the Atmospheric Sciences, 39, 2553–2564, https://doi.org/10.1175/1520-0469(1982)039<2553:SCOCAT>2.0.CO;2, 1982.

Båserud, L., Flügge, M., Bhandari, A., and Reuder, J.: Characterization of the SUMO turbulence measurement system for wind turbine wake assessment, Energy Procedia, 53, 173–183, https://doi.org/10.1016/j.egypro.2014.07.226, 2014.

405 Båserud, L., Reuder, J., Jonassen, M. O., Kral, S. T., Paskyabi, M. B., and Lothon, M.: Proof of concept for turbulence measurements with the RPAS SUMO during the BLLAST campaign, Atmospheric Measurement Techniques, 9, 4901–4913, https://doi.org/10.5194/amt-9-4901-2016, 2016.

Calmer, R., Roberts, G. C., Preissler, J., Sanchez, K. J., Derrien, S., and O'Dowd, C.: Vertical wind velocity measurements using a five-hole probe with remotely piloted aircraft to study aerosol-cloud interactions, Atmos. Meas. Tech, 11, 2583–2599, https://doi.org/10.5194/amt-

410 11-2583-2018, https://doi.org/10.5194/amt-11-2583-2018, 2018.

Chimonas, G.: Steps, waves and turbulence in the stably stratified planetary boundary layer, Boundary-Layer Meteorology, 90, 397–421, https://doi.org/10.1023/A:1001709029773, 1999.

Clayson, C. A. and Kantha, L.: On Turbulence and Mixing in the Free Atmosphere Inferred from High-Resolution Soundings, Journal of Atmospheric and Oceanic Technology, 25, 833–852, https://doi.org/10.1175/2007JTECHA992.1, https://journals.ametsoc.org/view/

415 journals/atot/25/6/2007jtecha992_1.xml, 2008.

Coulman, C. E.: Vertical profiles of small-scale temperature structure in the atmosphere, Boundary-Layer Meteorology, 4, 169–177, https://doi.org/10.1007/BF02265230, 1973.

Coulman, C. E., Vernin, J., and Fuchs, A.: Optical seeing—mechanism of formation of thin turbulent laminae in the atmosphere, Applied Optics, 34, 5461–5474, https://doi.org/10.1364/AO.34.005461, http://ao.osa.org/abstract.cfm?URI=ao-34-24-5461, 1995.

420 Dalaudier, F., Sidi, C., Crochet, M., and Vernin, J.: Direct Evidence of "Sheets" in the Atmospheric Temperature Field, Journal of the Atmospheric Sciences, 51, 237–248, https://doi.org/10.1175/1520-0469(1994)051<0237:DEOITA>2.0.CO;2, https://doi.org/10.1175/1520-0469(1994)051%3C0237:DEOITA%3E2.0.COhttp://0.0.0.2, 1994.

de Boer, gijS de Boer, Ivey, M., SChmid, B., dale LaWrenCe, darielle DexheiMer, Mei, F., john HuBBe, alBerT Bendure, jaSper HardeSTy, Shupe, M., alliSon MCCoMiSkey, hagen Telg, SChMiTT, C., MaTroSov, S., ian BrookS, jeSSie CreaMean, aMy SoloMon, david Turner,

425 WilliaMS, C., Maahn, M., ArgroW, B., Palo, S., Long, C., ru Shan Gao, jaMeS MaTher, de Boer, gijS de Boer, Ivey, M., SChMid, B., dale LaWrenCe, darielle DexheiMer, Mei, F., john HuBBe, alBerT Bendure, jaSper HardeSTy, Shupe, M., alliSon MCCoMiSkey, hagen Telg, SChMiTT, C., MaTroSov, S., ian BrookS, jeSSie CreaMean, aMy SoloMon, david Turner, WilliaMS, C., Maahn, M., ArgroW, B., Palo, S., Long, C., ru Shan Gao, and jaMeS MaTher: AFFILIATIONS: A BIRD'S-EYE VIEW Development of an Operational ARM Unmanned Aerial Capability for Atmospheric Research in Arctic Alaska, journals.ametsoc.org, 99, 1197–1212, https://doi.org/10.1175/BAMS-D-17-

430 0156.1, https://journals.ametsoc.org/doi/abs/10.1175/BAMS-D-17-0156.1, 2018.

de Boer, G., Diehl, C., Jacob, J., Houston, A., Smith, S. W., Chilson, P., Schmale, D. G., Intrieri, J., Pinto, J., Elston, J., Brus, D., Kemppinen, O., Clark, A., Lawrence, D., Bailey, S. C. C., Sama, M. P., Frazier, A., Crick, C., Natalie, V., Pillar-Little, E., Klein, P., Waugh, S., Lundquist, J. K., Barbieri, L., Kral, S. T., Jensen, A. A., Dixon, C., Borenstein, S., Hesselius, D., Human, K., Hall, P., Argrow, B., Thornberry, T., Wright, R., and Kelly, J. T.: Development of community, capabilities and understanding through unmanned aircraft-based

435 atmospheric research: The LAPSE-RATE campaign, Bulletin of the American Meteorological Society, https://doi.org/10.1175/bams-d-19-0050.1, 2019.

Doddi, A.: Insitu Sensing and Analysis of Turbulence - Investigation to Enhance Fine-Structure Turbulence Observation Capabilities of Autonomous Aircraft Systems, Ph.D. thesis, Ann Arbor, https://www.proquest.com/docview/2572553767?pq-origsite=gscholar&fromopenview=true#https://rp8jq9jy4s.search.serialssolutions.com?ctx_ver=Z39.88-2004&ctx_enc=info:ofi/enc:UTF-8&rfr_id=info:

440 sid/ProQuest+Dissertations+%26+Theses+Global&rft_val_fmt=info:ofi, 2021.

Eaton, F. D., Nastrom, G. D., Masson, B. S., Hahn, I. L., McCrae, K. A., Nowlin, S. R., and Berkopec, T. L.: Radar and aircraft observations of a layer of strong refractivity turbulence, in: Proc.SPIE, vol. 3381, https://doi.org/10.1117/12.323944, 1998.

Fairall, C. W., White, A. B., and Thomson, D. W.: A stochastic model of gravity-wave-induced clear-air turbulence, Journal of the Atmospheric Sciences, 48, 1771–1790, https://doi.org/10.1175/1520-0469(1991)048<1771:ASMOGW>2.0.CO;2, 1991.

445 Fernando, H. J. S., Pardyjak, E. R., Di Sabatino, S., Chow, F. K., De Wekker, S. F. J., Hoch, S. W., Hacker, J., Pace, J. C., Pratt, T., Pu, Z., Steenburgh, W. J., Whiteman, C. D., Wang, Y., Zajic, D., Balsley, B., Dimitrova, R., Emmitt, G. D., Higgins, C. W., Hunt, J. C. R., Knievel, J. C., Lawrence, D., Liu, Y., Nadeau, D. F., Kit, E., Blomquist, B. W., Conry, P., Coppersmith, R. S., Creegan, E., Felton, M., Grachev, A., Gunawardena, N., Hang, C., Hocut, C. M., Huynh, G., Jeglum, M. E., Jensen, D., Kulandaivelu, V., Lehner, M., Leo, L. S., Liberzon, D., Massey, J. D., McEnerney, K., Pal, S., Price, T., Sghiatti, M., Silver, Z., Thompson, M., Zhang, H., and Zsedrovits,

450 T.: The materhorn : Unraveling the intricacies of mountain weather, Bulletin of the American Meteorological Society, 96, 1945–1968, https://doi.org/10.1175/BAMS-D-13-00131.1, 2015.

Frehlich, R., Meillier, Y., Jensen, M. L., and Balsley, B.: Turbulence Measurements with the CIRES Tethered Lifting System during CASES-99: Calibration and Spectral Analysis of Temperature and Velocity, Journal of the Atmospheric Sciences, 60, 2487–

2495, https://doi.org/10.1175/1520-0469(2003)060<2487:TMWTCT>2.0.CO;2, https://doi.org/10.1175/1520-0469(2003)060%3C2487:
TMWTCT%3E2.0.COhttp://0.0.0.2, 2003.

Fritts, D. C. and Rastogi, P. K.: Convective and dynamical instabilities due to gravity wave motions in the lower and middle atmosphere: Theory and observations, Radio Science, 20, 1247–1277, https://doi.org/10.1029/RS020i006p01247, http://doi.wiley.com/10.1029/RS020i006p01247, 1985.

Fritts, D. C. and Wang, L.: Gravity wave-fine structure interactions. Part II: Energy dissipation evolutions, statistics, and implications, Journal of the Atmospheric Sciences, 70, 3735–3755, https://doi.org/10.1175/JAS-D-13-059.1, 2013.

Fritts, D. C., Wang, L., Werne, J., Lund, T., and Wan, K.: Gravity Wave Instability Dynamics at High Reynolds Numbers. Part I: Wave Field Evolution at Large Amplitudes and High Frequencies, Journal of the Atmospheric Sciences, 66, 1126–1148, https://doi.org/10.1175/2008JAS2726.1, https://journals.ametsoc.org/view/journals/atsc/66/5/2008jas2726.1.xml, 2009a.

Fritts, D. C., Wang, L., Werne, J., Lund, T., and Wan, K.: Gravity Wave Instability Dynamics at High Reynolds Numbers. Part II: Turbulence Evolution, Structure, and Anisotropy, Journal of the Atmospheric Sciences, 66, 1149–1171, https://doi.org/10.1175/2008JAS2727.1, https://journals.ametsoc.org/view/journals/atsc/66/5/2008jas2727.1.xml, 2009b.

Fritts, D. C., Wang, L., and Werne, J. A.: Gravity Wave–Fine Structure Interactions. Part I: Influences of Fine Structure Form and Orientation on Flow Evolution and Instability, Journal of the Atmospheric Sciences, 70, 3710–3734, https://doi.org/10.1175/JAS-D-13-055.1, http://journals.ametsoc.org/doi/abs/10.1175/JAS-D-13-055.1, 2013.

Fritts, D. C., Wang, L., Lund, T. S., and Thorpe, S. A.: Multi-Scale Dynamics of Kelvin-Helmholtz Instabilities . Part 1 : Secondary Instabilities and the Dynamics of Tubes and Knots, pp. 1–27, 2021a.

Fritts, D. C., Wang, L., Thorpe, S. A., and Lund, T. S.: Multi-Scale Dynamics of Kelvin-Helmholtz Instabilities . Part 2 : Energy Dissipation Rates , Evolutions , and Statistics, pp. 1–39, 2021b.

Fua, D., Chimonas, G., Einaudi, F., and Zeman, O.: ANALYSIS OF WAVE-TURBULENCE INTERACTION., Journal of the Atmospheric Sciences, 39, 2450–2463, https://doi.org/10.1175/1520-0469(1982)039<2450:AAOWTI>2.0.CO;2, 1982.

Gage, K. S. and Balsley, B. B.: On the scattering and reflection mechanisms contributing to clear air radar echoes from the troposphere, stratosphere, and mesophere, Radio Science, 15, 243–257, https://doi.org/10.1029/RS015i002p00243, https://doi.org/10.1029/RS015i002p00243, 1980.

Gage, K. S. and Green, J. L.: Evidence for specular reflection from monostatic VHF radar observations of the stratosphere, Radio Science, 13, 991–1001, https://doi.org/10.1029/RS013i006p00991, https://doi.org/10.1029/RS013i006p00991, 1978.

Gong, J. and Geller, M. A.: Vertical fluctuation energy in United States high vertical resolution radiosonde data as an indicator of convective gravity wave sources, Journal of Geophysical Research: Atmospheres, 115, https://doi.org/https://doi.org/10.1029/2009JD012265, https://doi.org/10.1029/2009JD012265, 2010.

Gossard, E. E., Chadwick, R. B., Detman, T. R., and Gaynor, J.: Capability of Surface-Based Clear-Air Doppler Radar for Monitoring Meteorological Structure of Elevated Layers, Journal of Climate and Applied Meteorology, 23, 474–485, https://doi.org/10.1175/1520-0450(1984)023<0474:COSBCA>2.0.CO;2, https://doi.org/10.1175/1520-0450(1984)023%3C0474:COSBCA%3E2.0.COhttp://0.0.0.2, 1984.

Hunt, J. C. R., Kaimal, J. C., and Gaynor, J. E.: Some observations of turbulence structure in stable layers, Quarterly Journal of the Royal Meteorological Society, 111, 793–815, https://doi.org/10.1002/qj.49711146908, https://doi.org/10.1002/qj.49711146908, 1985.

490   Kantha, L., Lawrence, D., Luce, H., Hashiguchi, H., Tsuda, T., Wilson, R., Mixa, T., and Yabuki, M.: Shigaraki UAV-Radar Experiment (ShUREX): overview of the campaign with some preliminary results, Progress in Earth and Planetary Science, 4, https://doi.org/10.1186/s40645-017-0133-x, 2017.

Kantha, L., Luce, H., Hashiguchi, H., and Doddi, A.: Atmospheric structures in the troposphere as revealed by high-resolution backscatter images from MU radar operating in range-imaging mode, Progress in Earth and Planetary Science, 6, 32, https://doi.org/10.1186/s40645-019-0274-1, https://doi.org/10.1186/s40645-019-0274-1, 2019.

495

Knievel, J. C., Liu, Y., Hopson, T. M., Shaw, J. S., Halvorson, S. F., Fisher, H. H., Roux, G., Sheu, R.-s., Pan, L., Hacker, J. P., Vernon, E., Gallagher Iii, F. W., and Pace, J. C.: Mesoscale Ensemble Weather Prediction at U.S. Army Dugway Proving Ground, Utah, journals.ametsoc.org, 32, 2195–2216, https://doi.org/10.1175/WAF-D-17-0049.1, www.ametsoc.org/PUBSReuseLicenses, 2017.

Kohma, M., Sato, K., Tomikawa, Y., Nishimura, K., and Sato, T.: Estimate of Turbulent Energy Dissipation Rate From the
500   VHF Radar and Radiosonde Observations in the Antarctic, Journal of Geophysical Research: Atmospheres, 124, 2976–2993, https://doi.org/https://doi.org/10.1029/2018JD029521, https://doi.org/10.1029/2018JD029521, 2019.

Lawrence, D. A. and Balsley, B. B.: Design of a low-cost UAS for high-resolution atmospheric sensing, in: AIAA Infotech at Aerospace (I at A) Conference, https://doi.org/10.2514/6.2013-4669, 2013.

Lawrence, D. A., Frew, E. W., and Pisano, W. J.: Lyapunov Vector Fields for Autonomous Unmanned Aircraft Flight Control, arc.aiaa.org,
505   31, 1220–1229, https://doi.org/10.2514/1.34896, http://arc.aiaa.org, 2008.

Liu, Y., Warner, T. T., Bowers, J. F., Carson, L. P., Chen, F., Clough, C. A., Davis, C. A., Egeland, C. H., Halvorson, S. F., Huck, T. W., Lachapelle, L., Malone, R. E., Rife, D. L., Sheu, R.-S., Swerdlin, S. P., and Weingarten @@, D. S.: The Operational Mesogamma-Scale Analysis and Forecast System of the U.S. Army Test and Evaluation Command. Part I: Overview of the Modeling System, the Forecast Products, and How the Products Are Used, journals.ametsoc.org, 47, 1077–1092, https://doi.org/10.1175/2007JAMC1653.1,
510   https://journals.ametsoc.org/doi/abs/10.1175/2007JAMC1653.1, 2008.

Luce, H., Kantha, L., Hashiguchi, H., Atmosphere, D. L., and undefined 2019: Estimation of Turbulence Parameters in the Lower Troposphere from ShUREX (2016–2017) UAV Data, mdpi.com, https://www.mdpi.com/2073-4433/10/7/384.

Luce, H., Crochet, M., Dalaudier, F., and Sidi, C.: Interpretation of VHF ST radar vertical echoes from in situ temperature sheet observations, Radio Science, 30, 1003–1025, https://doi.org/10.1029/95RS00713, https://doi.org/10.1029/95RS00713, 1995.

515   Luce, H., Fukao, S., Yamamoto, M., Sidi, C., and Dalaudier, F.: Validation of Winds Measured by MU Radar with GPS Radiosondes during the MUTSI Campaign, Journal of Atmospheric and Oceanic Technology, 18, 817–829, https://doi.org/10.1175/1520-0426(2001)018<0817:VOWMBM>2.0.CO;2, https://doi.org/10.1175/1520-0426(2001)018%3C0817:VOWMBM%3E2.0.COhttp://0.0.0.2, 2001.

Luce, H., Kantha, L., Hashiguchi, H., Lawrence, D., Yabuki, M., Tsuda, T., and Mixa, T.: Comparisons between high-resolution profiles of
520   squared refractive index gradient M 2 measured by the Middle and Upper Atmosphere Radar and unmanned aerial vehicles (UAVs) during the Shigaraki UAV-Radar Experiment 2015 campaign, 35, 423–441, https://doi.org/10.5194/angeo-35-423-2017, www.ann-geophys.net/35/423/2017/, 2017.

Luce, H., Kantha, L., Hashiguchi, H., Lawrence, D., and Doddi, A.: Turbulence kinetic energy dissipation rates estimated from concurrent UAV and MU radar measurements, Earth, Planets and Space, 70, https://doi.org/10.1186/s40623-018-0979-1, 2018a.

525   Luce, H., Kantha, L., Hashiguchi, H., Lawrence, D., Mixa, T., Yabuki, M., and Tsuda, T.: Vertical structure of the lower troposphere derived from MU radar, unmanned aerial vehicle, and balloon measurements during ShUREX 2015, Progress in Earth and Planetary Science, 5, https://doi.org/10.1186/s40645-018-0187-4, 2018b.

Luce, H., Kantha, L., Hashiguchi, H., and Lawrence, D.: Estimation of Turbulence Parameters in the Lower Troposphere from ShUREX (2016–2017) UAV Data, https://doi.org/10.3390/atmos10070384, 2019.

530 Mahrt, L.: Stratified Atmospheric Boundary Layers, Boundary-Layer Meteorology, 90, 375–396, https://doi.org/10.1023/A:1001765727956, https://doi.org/10.1023/A:1001765727956, 1999.

Muschinski, A. and Wode, C.: First In Situ Evidence for Coexisting Submeter Temperature and Humidity Sheets in the Lower Free Troposphere, Journal of the Atmospheric Sciences, 55, 2893–2906, https://doi.org/10.1175/1520-0469(1998)055<2893:FISEFC>2.0.CO;2, https://doi.org/10.1175/1520-0469(1998)055%3C2893:FISEFC%3E2.0.COhttp://0.0.0.2, 1998.

535 Muschinski, A., Frehlich, R., Jensen, M., Hugo, R., Hoff, A., Eaton, F., Balsley, B., Frehlich, R., Jensen, M., Hugo, R., Hoff, A., Eaton, F., and Balsley, B.: Fine-Scale Measurements Of Turbulence In The Lower Troposphere: An Intercomparison Between A Kite- And Balloon-Borne, And A Helicopter-Borne Measurement System, Boundary-Layer Meteorology, 98, 219–250, https://doi.org/10.1023/A:1026520618624, https://doi.org/10.1023/A:1026520618624, 2001a.

Muschinski, A., Frehlich, R., Jensen, M., Hugo, R., Hoff, A., Eaton, F., and Balsley, B.: Fine-scale measurements of turbulence in the
540 lower troposphere: An intercomparison between a kit-and balloon-borne, and a helicopter-borne measurement system, Boundary-Layer Meteorology, 98, 219–250, https://doi.org/10.1023/A:1026520618624, 2001b.

Parsons, D., Dabberdt, W., Cole, H., Hock, T., Martin, C., Barrett, A.-L., Miller, E., Spowart, M., Howard, M., Ecklund, W., Carters, D., Gage, K., and Wilson, J.: The Integrated Sounding System: Description and Preliminary Observations from TOGA COARE, Bulletin of the American Meteorological Society, 75, 553–568, https://doi.org/10.1175/1520-0477(1994)075<0553:TISSDA>2.0.CO;2, https://doi.
545 org/10.1175/1520-0477(1994)075%3C0553:TISSDA%3E2.0.COhttp://0.0.0.2, 1994.

Röttger, J.: Structure and dynamics of the stratosphere and mesosphere revealed by VHF radar investigations, pure and applied geophysics, 118, 494–527, https://doi.org/10.1007/BF01586465, https://doi.org/10.1007/BF01586465, 1980.

Röttger, J. and Liu, C. H.: Partial reflection and scattering of VHF radar signals from the clear atmosphere, Geophysical Research Letters, 5, 357–360, https://doi.org/10.1029/GL005i005p00357, https://doi.org/10.1029/GL005i005p00357, 1978.

550 Scipión, D. E., Lawrence, D. A., Milla, M. A., Woodman, R. F., Lume, D. A., and Balsley, B. B.: Simultaneous observations of structure function parameter of refractive index using a high-resolution radar and the DataHawk small airborne measurement system, ann-geophys.net, 34, 767–780, https://doi.org/10.5194/angeo-34-767-2016, www.ann-geophys.net/34/767/2016/, 2016.

Sidi, C., Lefrere, J., Dalaudier, F., and Barat, J.: An improved atmospheric buoyancy wave spectrum model, Journal of Geophysical Research: Atmospheres, 93, 774–790, https://doi.org/10.1029/JD093iD01p00774, https://doi.org/10.1029/JD093iD01p00774, 1988.

555 Smith, S. A., Fritts, D. C., and Vanzandt, T. E.: Evidence for a Saturated Spectrum of Atmospheric Gravity Waves, Journal of the Atmospheric Sciences, 44, 1404–1410, https://doi.org/10.1175/1520-0469(1987)044<1404:EFASSO>2.0.CO;2, https://doi.org/10.1175/1520-0469(1987)044%3C1404:EFASSO%3E2.0.COhttp://0.0.0.2, 1987.

Tatarskii, V. I.: The effects of the turbulent atmosphere on wave propagation, Jerusalem: Israel Program for Scientific Translations, 1971, 1971.

560 Tjernström, M., Balsley, B. B., Svensson, G., and Nappo, C. J.: The Effects of Critical Layers on Residual Layer Turbulence, Journal of the Atmospheric Sciences, 66, 468–480, https://doi.org/10.1175/2008JAS2729.1, https://doi.org/10.1175/2008JAS2729.1, 2009.

van den Kroonenberg, A., Martin, T., Buschmann, M., Bange, J., and Vörsmann, P.: Measuring the Wind Vector Using the Autonomous Mini Aerial Vehicle M2AV, Journal of Atmospheric and Oceanic Technology, 25, 1969–1982, https://doi.org/10.1175/2008JTECHA1114.1, https://doi.org/10.1175/2008JTECHA1114.1, 2008.

565   VanZandt, T. E., Green, J. L., Gage, K. S., and Clark, W. L.: Vertical profiles of refractivity turbulence structure constant: Comparison of observations by the Sunset Radar with a new theoretical model, Radio Science, 13, 819–829, https://doi.org/10.1029/RS013i005p00819, 1978.

Wildmann, N., Ravi, S., and Bange, J.: Towards higher accuracy and better frequency response with standard multi-hole probes in turbulence measurement with remotely piloted aircraft (RPA), Atmospheric Measurement Techniques, 7, 1027–1041, https://doi.org/10.5194/amt-7-
570   1027-2014, https://www.atmos-meas-tech.net/7/1027/2014/, 2014.

Wilson, R., Dalaudier, F., and Luce, H.: Can one detect small-scale turbulence from standard meteorological radiosondes?, Atmospheric Measurement Techniques, 4, 795–804, https://doi.org/10.5194/amt-4-795-2011, https://amt.copernicus.org/articles/4/795/2011/, 2011.

Witte, B. M., Schlagenhauf, C., Mullen, J., Helvey, J. P., Thamann, M. A., and Bailey, S.: Fundamental Turbulence Measurement with Unmanned Aerial Vehicles (Invited), in: 8th AIAA Atmospheric and Space Environments Conference, AIAA AVIATION Forum, American
575   Institute of Aeronautics and Astronautics, https://doi.org/doi:10.2514/6.2016-3584, https://doi.org/10.2514/6.2016-3584, 2016.

Woodman, R. F. and Chu, Y.: Aspect sensitivity measurements of VHF backscatter made with the Chung-Li radar: Plausible mechanisms, Radio Science, 24, 113–125, https://doi.org/10.1029/RS024i002p00113, 1989.

Woodman, R. F. and Guillen, A.: Radar Observations of Winds and Turbulence in the Stratosphere and Mesosphere, Journal of the Atmospheric Sciences, 31, 493–505, https://doi.org/10.1175/1520-0469(1974)031<0493:ROOWAT>2.0.CO;2, https://doi.org/10.1175/
580   1520-0469(1974)031%3C0493:ROOWAT%3E2.0.COhttp://0.0.0.2, 1974.

Woods, J. D.: Wave-induced shear instability in the summer thermocline, Journal of Fluid Mechanics, 32, 791–800, https://doi.org/10.1017/S0022112068001035, 1968.

Woods, J. D.: On Richardson's Number as a Criterion for Laminar-Turbulent-Laminar Transition in the Ocean and Atmosphere, Radio Science, 4, 1289–1298, https://doi.org/10.1029/RS004i012p01289, https://doi.org/10.1029/RS004i012p01289, 1969.
585   Xing-Sheng, L., Gaynor, J. E., and Kaimal, J. C.: A study of multiple stable layers in the nocturnal lower atmosphere, Boundary-Layer Meteorology, 26, 157–168, https://doi.org/10.1007/BF00121540, https://doi.org/10.1007/BF00121540, 1983.